The GluN2A Subunit of the NMDA Receptor Modulates the Rate of Functional Maturation in Parvalbumin-positive Interneurons

Chad R. Camp[1], Lindsey Shapiro[2], Anna Vlachos[3], Riley E. Perszyk[1], Nima Shariatzadeh[1], Jacob White[4], Russell Sanchez[4], Sookyong Koh[5], Andrew Escayg[2], Hongjie Yuan[1,6], Chris J. McBain[3], Kenneth A. Pelkey[3], Stephen F. Traynelis[1,6]

[1]Department of Pharmacology and Chemical Biology, Emory University School of Medicine, Atlanta, GA
[2]Department of Human Genetics, Emory University School of Medicine, Atlanta, GA
[3]Section on Cellular and Synaptic Physiology, Eunice Kennedy-Shriver National Institute of Child Health and Human Development, National Institutes of Health, Bethesda, MD
[4]Department of Pediatrics, Emory University School of Medicine, Atlanta, GA
[5]Omaha Children's Center, University of Nebraska Medical Center, Omaha, NE
[6]Center for Functional Evaluation of Rare Variants, Emory University School of Medicine, Atlanta, GA

Abstract

N-methyl-D-aspartate receptors (NMDARs) are excitatory glutamate-gated ion channels that are expressed throughout the central nervous system. NMDARs mediate calcium entry into cells, and are involved in a host of neurological functions, including neuronal development and maturation. The GluN2A subunit, encoded by the *GRIN2A* gene, has a slightly delayed expression pattern, with low transcript levels during embryonic development that peak in the early neonatal period. Given its unique expression pattern and ability to speed up the synaptic time course after incorporation into the postsynaptic density compared to other GluN2 subunits, the GluN2A subunit is well positioned to participate in synaptic maturation and circuit refinement. By using *Grin2a* knockout mice, we show that the loss of GluN2A signaling impacts parvalbumin-positive GABAergic interneuron development in the hippocampal CA1 subfield. Specifically, *Grin2a* knockout mice have 33% more parvalbumin-positive cells in CA1 compared to wild type controls, with no impact on cholecystokinin-positive cell density. By using immunohistochemical colocalization staining and electrophysiological recordings, we demonstrate that these excess parvalbumin cells do eventually incorporate into the hippocampal network and participate in phasic inhibition, although their presynaptic release probability may be dampened. Moreover, we show that although the morphology of *Grin2a* knockout parvalbumin-positive cells is unaffected, key measures of intrinsic excitability and action-potential firing properties show age-dependent alterations. Preadolescent (P20-25) parvalbumin-positive cells have an increased input resistance, longer membrane time constant, longer action-potential half-width, a lower current threshold for depolarization-induced block of action-potential firing, and a decrease in peak action-potential firing rate. Each of these electrophysiological measures becomes corrected in adulthood, reaching wild type levels, suggesting a delay of electrophysiological maturation. The circuit and behavioral implications of delayed parvalbumin-positive interneuron maturation are not known; however, we find that neonatal *Grin2a* knockout mice are more susceptible to lipopolysaccharide and febrile-induced seizures, consistent with a critical role for early GluN2A signaling in neuronal development and maintenance of excitatory-inhibitory balance. These results could provide insights into how loss-of-function *GRIN2A* human variants can generate an epileptic phenotype.

Introduction

N-methyl-D-aspartate receptors (NMDARs) comprise a family of ligand-gated ionotropic glutamate receptors that mediate a voltage-dependent, calcium-permeable component to fast excitatory neurotransmission (Hansen, Wollmuth et al. 2021). NMDARs are heterotetrameric assemblies composed of two obligate GluN1 subunits (encoded by the *GRIN1* gene) with two GluN2 subunits (encoded by the *GRIN2A-GRIN2D* genes) or two GluN3 subunits (encoded by the *GRIN3A* or *GRIN3B* genes) (Hansen, Wollmuth et al. 2021). Given their ubiquitous expression, participation in glutamatergic neurotransmission, and ability to allow facilitation of calcium entry into neurons, NMDARs have been implicated in a host of physiological and developmental roles including learning, memory, spatial navigation, coordinated movement, decision making, neuronal migration, morphological development, and synaptic connectivity (Collingridge 1987, Komuro and Rakic 1993, Watanabe, Inokawa et al. 1998, Nash and Brotchie 2000, Wang 2002, Nakazawa, McHugh et al. 2004, Ultanir, Kim et al. 2007, Adesnik, Li et al. 2008).

A growing volume of whole exome sequencing data implicates genetic variation within NMDARs as a contributing factor to several neuropathological conditions including epilepsy, schizophrenia, autism, intellectual disability, and developmental delay (Benke, Park et al. 2021, Garcia-Recio, Santos-Gomez et al. 2021). These genetic variants, which are absent from the healthy population, illustrate a critical role for NMDARs in basic and higher-level cognitive function (Perszyk, Myers et al. 2020, Amin, Moody et al. 2021). Moreover, when stratified by subunit, 43% (311/728) of all NMDAR genetic variants are within the *GRIN2A* gene, which encodes the GluN2A subunit (Benke, Park et al. 2021, Hansen, Wollmuth et al. 2021). Neurological conditions associated with *GRIN2A* variation present a range of symptoms, with the most common being epilepsy and intellectual delay, coupled with some form of aphasia (Carvill, Regan et al. 2013, Benke, Park et al. 2021, Hansen, Wollmuth et al. 2021). Although little is known about how mutations in the GluN2A protein contribute to neuropathology, functional evaluation of *GRIN2A* variants suggests that over half can be characterized as loss-of-function (LoF), as they diminish overall current flow through NMDARs or reduce receptor surface expression. These data suggest that diminished function from the GluN2A subunit may be sufficient to induce neurological disease, and this hypothesis is supported by data from *Grin2a* knockout (*Grin2a*$^{-/-}$) rodent models. *Grin2a*$^{-/-}$ mice have an array of neurological phenotypes including cortical epileptiform discharges, changes in anxiety-like and avoidance behaviors, deficits in spatial learning, changes in drug-seeking behaviors, and diminished pup ultrasonic vocalizations (Sakimura, Kutsuwada et al. 1995, Inoue, Mishina et al. 2003, Miyamoto, Yamada et al. 2004, Boyce-Rustay and Holmes 2006, Mozhui, Karlsson et al. 2010, Marquardt, Saha et al. 2014, Kannangara, Eadie et al. 2015, Salmi, Bolbos et al. 2018, Salmi, Del Gallo et al. 2019, Acutain, Griebler Luft et al. 2021).

The GluN2A subunit is found in both excitatory glutamatergic pyramidal cells and inhibitory GABAergic interneurons, as well as several other cell types such as dopaminergic and serotonergic neurons (Perszyk, DiRaddo et al. 2016, Hansen, Wollmuth et al. 2021). GluN2A is temporally regulated, with relatively low expression during the late embryonic and early postnatal periods that increases during preadolescence and is sustained into adulthood (Akazawa, Shigemoto et al. 1994, Monyer, Burnashev et al. 1994). GluN2A's function in rodent pyramidal cells has been extensively studied, where it helps shape the time-course of NMDAR-mediated excitatory postsynaptic currents (EPSCs) and provides a supportive function to long-term potentiation (Bard and Groc 2011, Paoletti, Bellone et al. 2013, Shipton and Paulsen 2014). Moreover, a switch in expression of GluN2B-to-GluN2A that changes the ratio of synaptic GluN2B:GluN2A during early postnatal development is well characterized in pyramidal cells, and may represent a stage in circuit maturation (Sheng, Cummings et al. 1994, Barria and Malinow 2002, Gray, Shi et al. 2011). GluN2A mRNA is expressed in multiple interneuron subtypes of both the medial and caudal ganglionic eminences (Perszyk, DiRaddo et al. 2016), however, interneurons from the medial ganglionic eminence (MGE) generally express more GluN2A and show a prominent GluN2B-to-GluN2A switchover compared to interneurons from the caudal ganglionic eminence (CGE) (Matta, Pelkey et al. 2013). Moreover, specific

antagonism or targeted knockdown of the GluN1, GluN2B, or GluN2D subunits of NMDARs impede interneuron development, suggesting an active role for NMDARs in interneuron maturation (Hanson, Weber et al. 2013, Kelsch, Li et al. 2014, Chittajallu, Wester et al. 2017, Hanson, Armbruster et al. 2019). Given the expression of GluN2A in interneurons, we hypothesized that GluN2A signaling may also play an active role in early interneuron development, thereby explaining some *GRIN2A* variant-associated phenotypes.

Here, we investigate the role of GluN2A in interneuron migration, synaptic connectivity, phasic inhibition, morphology, intrinsic excitability, and action-potential firing properties using *Grin2a*$^{-/-}$ mice. These experiments were conducted during preadolescence – a period right after the GluN2B-to-GluN2A switch (Matta, Pelkey et al. 2013) – and adulthood to assess whether any aberrations in *Grin2a*$^{-/-}$ mice are transient. While global homozygous knockout mice do not fully reproduce the effects of human LoF variants, data from this study provide a deeper understanding of GluN2A's role in circuit function and interneuron maturation and emphasize the critical importance of early GluN2A signaling in the developing brain.

Results

GABAergic Interneuron Cell Density in the Mouse Hippocampus

GABAergic interneurons infiltrate the developing hippocampus late during embryonic development, with nearly half dying off during the first postnatal week (Tricoire, Pelkey et al. 2011, Southwell, Paredes et al. 2012). Given the high expression levels of NMDARs during the embryonic and early postnatal periods, a loss of GluN2A signaling could generate aberrant interneuron cell density counts if NMDARs are involved in determination of interneuron survival. There are several interneuron subtypes in the hippocampus, with parvalbumin^{+} (PV) and cholecystokinin^{+} (CCK) interneurons accounting for the majority of GABAergic interneurons in this region (Pelkey, Chittajallu et al. 2017). PV and CCK cells have opposing transcriptomic profiles and each represents a major subtype of interneuron arising from the MGE and CGE, respectively (Pelkey, Chittajallu et al. 2017).

As evident from Figure 1, the loss of *Grin2a* causes a significant increase in PV cell density in CA1 (Figure 1B; 4875 ± 162 WT vs 6488 ± 276 *Grin2a*$^{-/-}$ cells per mm^3; p=0.00003, Student's two-sample t-test) of preadolescent mice. This increase is sustained into adulthood (Figure 1D; 4436 ± 326 WT vs 6212 ± 505 *Grin2a*$^{-/-}$ cells per mm^3; p=0.0055, Student's two-sample t-test). There is no difference in CA3 PV cell density at either age (Figure 1B and 1D) or in PV cell density in the somatosensory cortex in *Grin2a*$^{-/-}$ mice at either age (Supplemental Figure 1J). The loss of *Grin2a* does not change CA1 CCK cell density in preadolescent or adult mice (Figure 1F and 1H). In the CA3, there is also no difference in CCK cell density in preadolescent mice (Figure 1F), with a slight decrease in CA3 CCK cell density in *Grin2a*$^{-/-}$ adult mice (Figure 1H). The lack of effect on CCK interneuron cell density in *Grin2a*$^{-/-}$ mice is consistent with these interneurons having significantly less GluN2A expression than PV cells (Matta, Pelkey et al. 2013, Perszyk, DiRaddo et al. 2016).

Despite an increase in cell density, the overall lamination pattern of PV cells in CA1 is not disrupted by the loss of *Grin2a* (Supplemental Figures 1B and 1D) at either age, with the majority of PV cells found in the *stratum pyramidale* and *stratum oriens* layers as previously reported (Pelkey, Chittajallu et al. 2017). We also report that there are no differences in CCK CA1 lamination at either age (Supplemental Figures 1F and 1H). These data indicate that the loss of *Grin2a* may preferentially impact MGE-derived interneuron infiltration, survival, or apoptosis in the hippocampus.

GABAergic Interneuron Synaptic Density in CA1

After their programmed cell death, hippocampal GABAergic interneurons begin to incorporate into the network and establish numerous synaptic connections during the first week of postnatal development (De Felipe, Marco et al. 1997). To

determine whether the loss of *Grin2a* interferes with these processes, we assessed GABAergic synaptic density in CA1 via immunohistochemical colocalization of presynaptic and postsynaptic proteins which comprise GABAergic synapses. We first probed for the total number of GABAergic synapses by staining for vGAT (a presynaptic protein) and gephyrin (a postsynaptic protein). In preadolescent mice, there is a significant increase in vGAT/gephyrin colocalized puncta in the *stratum pyramidale* (0.0.6 ± 0.01 WT vs 0.08 ± 0.01 *Grin2a*$^{-/-}$ synapses per µm^3; p=0.0347, Student's two-sample t-test; Figure 2G) but not in the *stratum radiatum* (Figure 2H) of *Grin2a*$^{-/-}$ mice. This increase in GABAergic synaptic density is continued into adulthood, with significantly increased densities in both *stratum pyramidale* (0.11 ± 0.01 WT vs 0.15 ± 0.01 *Grin2a*$^{-/-}$ synapses per µm^3; p=0.0032, Student's two-sample t-test; Figure 2G) and *stratum radiatum* (0.13 ± 0.01 WT vs 0.16 ± 0.01 *Grin2a*$^{-/-}$ synapses per µm^3; p=0.025, Student's two-sample t-test; Figure 2H) in *Grin2a*$^{-/-}$ mice. See Supplemental Figure 2 and Table 2 for individual puncta counts and values, respectively. These data suggest that *Grin2a*$^{-/-}$ mice have increased levels of GABAergic synaptic densities in CA1.

Given that the number of PV cells in the CA1 subfield is increased in *Grin2a*$^{-/-}$ mice, we probed for PV cell-specific synaptic density. As previously reported, synaptotagmin II (SytII) is a reliable and specific presynaptic marker of PV cell boutons (Sommeijer and Levelt 2012). Thus, PV cell-mediated synapses can be assessed by probing for the colocalization of SytII (a presynaptic protein) and gephyrin (a postsynaptic protein). In preadolescent mice, there is no difference in SytII/gephyrin colocalized puncta in the *stratum pyramidale* (Figure 3G) or in the *stratum radiatum* (Figure 3H) of *Grin2a*$^{-/-}$ mice. In adult mice, PV cell-specific synaptic density is significantly increased in both *stratum pyramidale* (0.08 ± 0.01 WT vs 0.12 ± 0.01 *Grin2a*$^{-/-}$ synapses per µm^3; p=0.0028, Student's two-sample t-test; Figure 3G) and *stratum radiatum* (0.06 ± 0.01 WT vs 0.09 ± 0.01 *Grin2a*$^{-/-}$ synapses per µm^3; p=0.0094, Student's two-sample t-test; Figure 3H) in *Grin2a*$^{-/-}$ mice. See Supplemental Figure 3 and Table 2 for individual puncta counts and values, respectively. These data suggest that *Grin2a*$^{-/-}$ mice have increased levels of PV cell-specific synaptic densities in CA1, likely stemming from excess PV cells as reported in Figure 1.

Morphological Profile of CA1 PV Cells

Given the apparent increase in PV-cell mediated synaptic density in adult *Grin2a*$^{-/-}$ mice and that genetic deletion of NMDAR subunits can impact interneuron morphology (De Marco Garcia, Priya et al. 2015, Chittajallu, Wester et al. 2017, Hanson, Armbruster et al. 2019), we probed for changes in dendritic and axonal branching and placement by analyzing 3D reconstructions of biocytin backfilled CA1 PV cells. We observed no detectable changes in total length of dendrites or axons (Figure 4E) or in the total number of sholl intersections in dendrites or axons (Figure 4F) in preadolescent CA1 PV cells from either genotype. Sholl profiles of both dendrites (Figure 4G) and axons (Figure 4H) from preadolescent CA1 PV cells are also unchanged across genotype. The placement of both dendrites (Figure 4I) or axons (Figure 4J) assessed via polar plots showed no differences, with equal axonal placement in both the vertical and horizontal planes throughout *stratum pyramidale* (Figure 4K). Given that we showed no differences in CA1 PV cells from preadolescent *Grin2a*$^{-/-}$ mice, and that is it unlikely for cellular morphology to measurably change after preadolescent development, morphology in adult CA1 PV cells was not evaluated. Additionally, the absence of changes in PV cell morphology, combined with an increased PV-cell mediated synaptic density, suggests that the excess PV cells observed in *Grin2a*$^{-/-}$ mice may synaptically incorporate into the hippocampal network, and do not appear to make ectopic synaptic connections.

Phasic Inhibition onto CA1 Pyramidal Cells

Although the number of GABAergic interneurons in the hippocampus are significantly less than their pyramidal cell counterparts, these cells exert a profound control over network excitability and output (Pelkey, Chittajallu et al. 2017). This is accomplished via several different mechanisms, including setting the phasic inhibitory tone via stochastic GABA release onto

pyramidal cells (Farrant and Nusser 2005). To measure phasic inhibitory tone, we recorded miniature inhibitory postsynaptic currents (mIPSCs) onto CA1 pyramidal cells. There is no difference in *Grin2a*$^{-/-}$ mIPSC frequency compared to age-matched WT preadolescent and adult mice (Figure 5E). The cumulative distribution plots of mIPSC inter-event intervals in preadolescent (Figure 5F) and adult (Figure 5G) mice are significantly different between *Grin2a*$^{-/-}$ and wild type mice. We did not observe any difference in mIPSC amplitude (Figure 5H; Supplemental Figures 5H and 5I) or mIPSC time course (Supplemental Figures 5C-E) between *Grin2a*$^{-/-}$ and wild type mice at either age.

As previously reported, mIPSCs onto pyramidal cells are largely from basket cell interneuron activity, which in the hippocampus arises from approximately equal contributions from PV and CCK basket cells (Soltesz, Smetters et al. 1995, Akgul, Abebe et al. 2019). In order to probe PV cell-specific activity, we bath applied DAMGO, a specific mu-opioid receptor agonist (Onogi, Minami et al. 1995). Mu opioid receptors are found preferentially on the presynaptic boutons of PV cells, and DAMGO application eliminates PV cell-mediated GABA release onto CA1 pyramidal cells (Drake and Milner 2002, Shao, Chen et al. 2020). For these experiments, five minutes of baseline activity was established before 1 µM DAMGO was bath applied to the slice for seven minutes (Figure 5M and 5N). The last two minutes of DAMGO application were analyzed and compared to the baseline period. As evident from Figure 5O, the percent DAMGO inhibition of mIPSC frequency was nearly 50% in *Grin2a*$^{-/-}$ and WT mice at both ages. DAMGO did not alter other features of mIPSCs (Supplemental Figure 4). These data suggest that the overall contribution of basket PV cell activity is unchanged following the loss of *Grin2a*, despite *Grin2a*$^{-/-}$ mice harboring more PV cell-specific synaptic connections.

Passive and Action-Potential Firing Properties of CA1 PV Cells

In addition to providing action potential-independent tone, GABAergic interneurons largely orchestrate network activity via precise spatiotemporally controlled action potential-dependent neurotransmission following recruitment by excitatory afferent input. To assess PV cell excitability, we examined a handful of passive electrical properties. We report no changes in resting membrane potential (Figure 6B) or capacitance (Figure 6C) in PV cells of preadolescent or adult mice from either genotype. We do see a transient increase in preadolescent *Grin2a*$^{-/-}$ mice in both PV cell input resistance (Figure 6D; 96.0 ± 7.9 WT vs 149 ± 15 *Grin2a*$^{-/-}$ MΩ; p=0.0032, Student's two-sample t-test) and membrane time constant (Figure 6F; 11 ± 0.9 WT vs 17 ± 1.9 *Grin2a*$^{-/-}$ ms; p=0.0058, Student's two-sample t-test). Both measures return to normal, WT levels in adult mice (Figure 6D and 6F). We also examined several features of PV cell action potential firing characteristics to determine how efficiently these cells transmit electrical signals. While we observed no change in rheobase in preadolescent or adult mice from either genotype (Figure 6G), we do see a transient prolongation of the action potential half-width in preadolescent mice (Figure 6H; 0.49 ± 0.01 WT vs 0.65 ± 0.05 *Grin2a*$^{-/-}$ ms; p=0.0018, Student's two-sample t-test) that returns to WT levels in adulthood. Other features of the action potential waveform appear unchanged regardless of age or genotype (See Supplemental Table 5). The sum of these data suggests that the loss of the GluN2A subunit causes a transient delay in the electrophysiological maturation of PV cells in the mouse hippocampus, although the exact temporal resolution of said changes are undefined.

Another important feature of interneurons, especially PV cells, is their ability to respond to and transmit rapid electrical signals under heavy excitatory afferent recruitment. The fast-spiking nature of PV cells is critical for regulating pyramidal cell and network activity, where they modulate spiking probability and contribute heavily to gamma oscillations (Hu, Gan et al. 2014). To test the efficiency with which PV cells fire action-potentials and respond to strong depolarization, we measured the current required to reach depolarization-induced block and the maximum action potential firing frequency before depolarization-induced block. Both the threshold for depolarization-induced block (Figure 6J; 1374 ± 98 WT vs 761 ± 106 *Grin2a*$^{-/-}$ pA; p=0.0001, Student's two-sample t-test) and maximum firing frequency before block (Figure 6L; 268 ± 13 WT vs 186 ± 15 *Grin2a*$^{-/-}$ Hz; p=0.0002, Student's two-sample t-

test) were transiently decreased in preadolescent *Grin2a*$^{-/-}$ mice. Both measures could have profound consequences on circuit excitability and network wiring during the critical plasticity period in preadolescent development, which may manifest as epileptiform activity, maladaptive plasticity, or cognitive impairment.

Seizure Profile of Grin2a$^{-/-}$ *Mice During Development*

Given that *Grin2a*$^{-/-}$ mice have profound deficits in PV cell function and that *Grin2a*$^{-/-}$ mice have been reported to have epileptiform activity, we assessed seizure susceptibility in several models of hypersynchronous activity in neonatal and adult mice (Salmi, Bolbos et al. 2018). We first looked at lipopolysaccharide and fever-induced seizures in neonatal mice, as febrile seizures can be indicative of early signs of epilepsy (Nelson and Ellenberg 1976). By injecting mice with 0.1 mg/kg lipopolysaccharide 2 hours before gradual heating, we can simulate a bacterial infection-induced fever, which promotes seizure activity in rodents (Eun, Abraham et al. 2015). As evident from Figure 7B, neonatal *Grin2a*$^{-/-}$ are significantly more susceptible to lipopolysaccharide and fever-induced generalized tonic-clonic seizures compared to age-matched WT controls (3/19 WT mice vs 13/17 *Grin2a*$^{-/-}$ mice; p=0.0003, chi-squared test). There are also no differences in baseline temperature two hours after lipopolysaccharide injection (Supplemental Figure 7A) or in temperature attained at (Figure 7C) or latency to (Figure 7D) generalized tonic-clonic seizure after heating. Next, to investigate how a delayed maturation of PV cell electrophysiological properties may impact circuit excitability, we assessed seizure susceptibility in adult mice using the chemoconvulsants pentylenetetrazol and flurothyl. Adult *Grin2a*$^{-/-}$ mice showed no differences in latency to generalized tonic-clonic seizure after 100 mg/kg subcutaneous pentylenetetrazol injection (Figure 7E), in a pentylenetetrazol injection survival plot (Figure 7F), or after exposure to 20 µL/min flurothyl inhalation (Figure 7G). There are no observable sex differences in latency to generalized tonic-clonic seizure after pentylenetetrazol injection (Supplemental Figure 7B and 7C) or flurothyl inhalation (Supplemental Figure 7D and 7E) in either genotype. An electrical corneal stimulation paradigm (6 Hz) was used to uncover potential changes in limbic system excitability given that much of our data was obtained from hippocampus. *Grin2a*$^{-/-}$ mice were more resistant to 6 Hz-induced seizures compared to WT mice (Figure 7H; median Racine score 2 for WT vs 0 for *Grin2a*$^{-/-}$; p=0.000001, Mann-Whitney test), with no apparent sex-differences (Figure 7I and Figure 7J). These data suggest that *Grin2a*$^{-/-}$ show signs of altered network excitability in both neonates and adults.

Discussion

The data we report here suggest multiple potential roles for the GluN2A subunit of NMDARs in the regulation of development and maturation of GABAergic interneurons in the mouse hippocampus. Specifically, we report that full loss of the *Grin2a* gene, encoding the GluN2A subunit, causes aberrations in PV cell density, synaptic connectivity, passive intrinsic properties, and action potential firing characteristics. While it was reported that *Grin2a*$^{-/-}$ mice have changes in glutamatergic cells, this study provides crucial evidence that the loss of GluN2A also impacts PV interneurons (Kannangara, Bostrom et al. 2014). Using *Grin2a*$^{-/-}$ mice, we demonstrated that NMDAR-mediated signaling impacts interneuron cell density, providing supportive evidence for the potential influence of early electrical or metabotropic NMDAR-mediated signaling in interneuron survival and/or apoptosis. Extra PV cells from the loss of *Grin2a*$^{-/-}$ incorporate into the hippocampal network as assessed via synaptic colocalization staining and Sholl analysis, suggesting that GluN2A-mediated signaling may not be involved in PV cell-mediated synaptogenesis or morphological development. Despite increased synaptic density, we report no changes in mIPSC frequency in *Grin2a*$^{-/-}$ mice, which may be explained by changes to presynaptic release probability or by changes in the number of functional synapses. We also show that NMDAR-mediated signaling may be sufficient, but not necessary, to initiate a series of genetic programs which controls cellular excitability and electrophysiological maturation of hippocampal PV cells (Mahadevan, Mitra et al. 2021).

In addition to uncovering some unique potential mechanisms of PV cell maturation, this study highlights a critical role for early GluN2A signaling in neurodevelopment. The role of NMDARs in neuronal development has been appreciated for decades, with attention mostly directed at the GluN2B and GluN2D subunits (Wang, Held et al. 2011, Kelsch, Li et al. 2014, Yamasaki, Okada et al. 2014, Jiang, Jiang et al. 2015, Hanson, Armbruster et al. 2019). The GluN2A subunit, with its surge in postnatal expression at week two of rodent development, has largely been considered an adolescent and adult subunit, often associated with synapse maturation in principal cells and overall circuit refinement (Dumas 2005, Gray, Shi et al. 2011). Incorporation of GluN2A into the postsynaptic density accelerates the NMDAR-mediated synaptic time course, generating briefer but more efficient dendritic calcium transients (Evans, Morera-Herreras et al. 2012). Even though hippocampal mRNA levels of GluN2A are low before P14, interneuron survival/apoptosis is largely decided before the GluN2A's increased expression around P14 (Tricoire, Pelkey et al. 2011, Matta, Pelkey et al. 2013). Additionally, WT CA1 PV cells at P20-25 already displayed signs of electrophysiological maturation suggesting that GluN2A's influence on genetic programs controlling cellular excitability and action-potential firing likely happen at or before GluN2A's increased expression. These deficits are likely not due to a complete loss of NMDAR-mediated signaling in PV cells, as *Grin2a*$^{-/-}$ rodent models have similar NMDAR-mediated excitatory postsynaptic current amplitudes to age-matched WT cells (Booker, Sumera et al. 2021). Although their NMDAR-mediated current amplitudes are similar, *Grin2a*$^{-/-}$ PV cells have a prolongation of NMDAR-mediated synaptic time course, as would be expected for neurons expressing only GluN2B- and GluN2D-containing NMDARs (Booker, Sumera et al. 2021, Hansen, Wollmuth et al. 2021). A prolongation of the NMDAR-mediated synaptic time course would likely drive more calcium into the cell and impact numerous genetic programs. Whether PV cell apoptosis and electrophysiological maturation are signaled by changes in postsynaptic calcium transients mediated by GluN2A insertion, or by metabotropic processes occurring on the C-terminal tail of the GluN2A subunit remains unknown. Alternatively, changes observed in PV cell maturation may be due to non-cell autonomous alterations in pyramidal cell signaling onto PV cells or changes in overall network state due to a loss of global GluN2A signaling.

The circuit ramifications of these PV interneuron deficits are unexplored. Several studies have reported that *Grin2a*$^{-/-}$ mice display a range of aberrant phenotypes, including epileptiform cortical discharges and deficits in spatial learning (Sakimura, Kutsuwada et al. 1995, Salmi, Bolbos et al. 2018). These changes in circuit function could be explained by preadolescent *Grin2a*$^{-/-}$ PV cells experiencing depolarization-induced block at lower current thresholds than age-matched WT mice. Experimentally limiting depolarization-induced block in CA1 PV cells, researchers halted evoked hippocampal epileptiform activity and restored normal pyramidal cell firing (Calin, Ilie et al. 2021). We show that diminished PV cell function generates a transient lipopolysaccharide and febrile-induced seizure vulnerability window in neonatal *Grin2a*$^{-/-}$ mice, while adult *Grin2a*$^{-/-}$ mice display a resistance to 6 Hz-induced seizures. While a higher threshold to electrically induced seizures in adults is unexpected, these data are in line with a recent study evaluating a gain-of-function GluN2A mutant mouse model that reported similar protection from 6 Hz-induced seizures, despite these mice having an epileptic phenotype (Amador, Bostick et al. 2020). Moreover, the bulk of PV cell dysfunction happens during the critical plasticity period in *Grin2a*$^{-/-}$ mice, with altered levels of PV-mediated feedforward inhibition potentially causing multiple circuit-level changes. Increased neonatal seizure vulnerability and aberrant seizure thresholds in adults, however, are consistent with reduced GluN2A function as one factor contributing to seizure occurrence in patients with *GRIN2A* LoF variants.

Increased Parvalbumin Cell Density

GABAergic interneurons mostly arise from one of two major stem cell populations – the MGE and CGE. All PV cells arise from MGE progenitors and all CCK cells arise from CGE progenitors (Pelkey, Chittajallu et al. 2017). As reported, the loss of *Grin2a* only impacts CA1 PV cell density, suggesting that MGE-derived interneurons may by preferentially impacted by the loss of GluN2A. Cortical and hippocampal MGE interneuron fate is largely controlled by the early embryonic transcription factor *Nkx2.1*, responsible

for initiating a series of determinate genetic programs (Sussel, Marin et al. 1999, Butt, Sousa et al. 2008, Tricoire, Pelkey et al. 2010). Given that we reported no changes in cortical PV cell density, it is unlikely, although not impossible, that the loss of *Grin2a* is affecting *Nkx2.1*-derived intrinsic genetic programs and increasing the number of MGE-derived interneurons generated. Instead, our data suggest that the loss of GluN2A may be impacting interneuron survival or apoptosis, other critical factors in determining overall cell density. After interneuron infiltration, nearly half will undergo apoptosis, fine-tuning the balance of pyramidal cells to interneurons (Southwell, Paredes et al. 2012). The exact mechanisms of interneuron apoptosis are not fully understood, but are likely controlled by a combination of internal genetic cues, external neurotropic factors, and early interneuron electrical activity (Southwell, Paredes et al. 2012, Denaxa, Neves et al. 2018, Priya, Paredes et al. 2018). Recent data suggests that interneuron apoptosis, especially in CCK and PV cells, is mostly controlled by electrical activity and most importantly via calcium influx (Denaxa, Neves et al. 2018, Priya, Paredes et al. 2018). However, the extent to which local electrical signaling, especially from NMDARs, within PV interneurons controls pro-apoptotic pathways has not been determined.

Why is PV cell density, but not CCK cell density, impacted by the loss of *Grin2a*? NMDARs are found on both PV and CCK cells, however, recent reports suggest that CCK cells express less GluN2A than their PV cell counterparts (Matta, Pelkey et al. 2013, Perszyk, DiRaddo et al. 2016, Booker, Sumera et al. 2021). Additionally, CCK cell density is reportedly influenced by 5-HT_{3A} and AMPA receptor-mediated activity (Murthy, Niquille et al. 2014, Akgul, Abebe et al. 2019). Despite having a higher overall synaptic NMDA:AMPA, perhaps CCK cells rely on electrical cues from non-NMDARs to control apoptotic pathways (Bortone and Polleux 2009, Matta, Pelkey et al. 2013). Alternatively, since CCK cells have limited GluN2A expression, the loss of this subunit could have minimal impact on NMDAR-mediated apoptosis in this interneuron subtype. Future experiments should focus on elucidating the impact of early NMDAR signaling regarding initiating interneuron apoptosis in both MGE- and CGE-derived interneurons.

Age-Dependent Increases in Synaptic Connectivity, but No Change in Phasic Inhibition

During interneuron hippocampal infiltration and radial lamination, robust synaptogenesis begins, with the earliest interneuron-mediated synaptic connections being reported between E18-P2 (Owens, Liu et al. 1999, Tyzio, Represa et al. 1999). The number of GABAergic inhibitory synapses steadily increases until P30-35 or until mice reach adolescence (De Felipe, Marco et al. 1997). After adolescence and into early adulthood, GABAergic synapses undergo activity-dependent pruning, reaching steady-state levels around P50-60 (De Felipe, Marco et al. 1997, Lin, Bloodgood et al. 2008). In this study, we used a distance-based colocalization of various presynaptic and postsynaptic markers of GABAergic synapses to estimate synaptic density in the *stratum pyramidale* and *stratum radiatum* of the CA1 subfield. We report that the overall synaptic density is lower in both CA1 subfield layers in preadolescence compared to adulthood, regardless of genotype. However, a more rigorous time scale of synaptic density counts would be needed to determine at what age peak synaptic density occurs and to make conclusions regarding preadolescent versus adult synaptic counts.

By using synaptotagmin II, a presynaptic protein specific for mature PV presynaptic boutons, we were able to estimate the number of synaptic connections made by PV interneurons (Sommeijer and Levelt 2012). In hippocampus, SytII preferentially labels PV basket cells, with limited labeling of PV bistratified and PV axo-axonic cells, suggesting that much of our synaptic colocalization data are from PV basket cells. (Garcia-Junco-Clemente, Cantero et al. 2010). In both WT and *Grin2a*$^{-/-}$ mice, the overall PV-mediated synaptic density is greater in the *stratum radiatum* than *stratum pyramidale* in preadolescence, with these number evening out in adulthood. These data are in agreement with a recent study showing that immature PV basket cells start off by making synaptic connections on the proximal apical dendrites of pyramidal cells (Micheva, Kiraly et al. 2021). As PV basket cells age, their synaptic connections are refined and begin migrating to the soma where they exert strong inhibitory control on pyramidal cell firing (Royer,

Zemelman et al. 2012, Micheva, Kiraly et al. 2021). Thus, in adulthood we are likely capturing a large extent of PV basket cells in the *stratum pyramidale* layer and some synaptic connectivity from PV bistratified and basket cells in the *stratum radiatum*. We also report that the overall number of GABAergic and PV-mediated synaptic connections are significantly increased in adult *Grin2a*$^{-/-}$ mice. Since *Grin2a*$^{-/-}$ mice also have an increased PV cell density in the CA1 subfield, this increased synaptic density is likely a product of excess PV cells forming synaptic connections and incorporating into the hippocampal network. Given the limited SytII labeling outside of hippocampal PV basket cells, detailed morphological and retrograde tracing analyses of PV bistratified and axo-axonic cells would be needed to determine whether the loss of *Grin2a* has an impact on their synaptic connectivity.

While presynaptic and postsynaptic protein colocalization can provide estimates for synaptic density, they do not provide any evidence on whether visualized synapses are functional. To address this issue, we recorded mIPSCs onto CA1 pyramidal cells. mIPSC recordings, made in the presence of the voltage-gated sodium channel blocker tetrodotoxin, provide action potential-independent synaptic events that result from stochastic calcium entry into presynaptic boutons (Goswami, Bucurenciu et al. 2012). More specifically, mIPSCs are thought to represent single quantal events from individual synapses, allowing for estimations of presynaptic release probability, synaptic connectivity, and overall phasic inhibitory tone (Ropert, Miles et al. 1990, Farrant and Nusser 2005, Goswami, Bucurenciu et al. 2012). However, since pyramidal cells are so large and mIPSC recordings are largely single quantal events, most mIPSC data represent synaptic activity from basket cells since mIPSCs arising from more distal inputs will undergo strong electrotonic filtering, often falling below our detection threshold (Soltesz, Smetters et al. 1995). There are no detectable changes in mIPSC frequency and amplitude in both preadolescent and adult mice from WT and *Grin2a*$^{-/-}$ mice. Since most mIPSCs arise from both PV and CCK soma-synapsing basket cells, we used the selective mu opioid receptor agonist DAMGO to silence PV-cell mediated mIPSCs (Onogi, Minami et al. 1995, Lau, Ambrose et al. 2020). Percent DAMGO inhibition was unchanged in both preadolescent and adult mice from WT and *Grin2a*$^{-/-}$ mice. Taken together, the loss of GluN2A does not change mIPSC frequency or PV cell-mediated mIPSC frequency despite *Grin2a*$^{-/-}$ mice having an increased PV cell-mediated synaptic density. There are multiple possible interpretations of these data, with one being that the loss of GluN2A diminishes presynaptic release probability. Presynaptic NMDARs on PV cell boutons have been reported but how they are activated and their involvement in modulating GABA release is not clear (Pafundo, Miyamae et al. 2018). Alternatively, the loss of GluN2A could generate two different pools of synapses, one with an increased presynaptic release probability and others with release probabilities near zero. Future studies investigating the possibility of presynaptic NMDARs modulating GABA release and those investigating individual synaptic release probability would be required to definitively answer these questions.

Age-Dependent Alterations to Passive and Action Potential Firing Properties

In addition to providing phasic inhibition, GABAergic interneurons also participate in action-potential dependent neurotransmission. PV cells are known for their fast-spiking action potential characteristics, which can generate gamma oscillations that are involved in higher-order cognitive function (Crone, Sinai et al. 2006, Sohal, Zhang et al. 2009). By examining both passive intrinsic properties and action potential firing characteristics, we can estimate how these cells may perform under synaptic load and how efficiently they can transduce somatic depolarizations into signal-carrying action potentials. The loss of *Grin2a* in preadolescent mice is associated with a host of electrophysiological changes, including an increased input resistance, a prolonged membrane time constant, and longer action potential half-widths. Each of these electrophysiological measures are known to be age-dependent, with PV cells in neonatal mice displaying a higher input resistance, longer membrane time constant, and longer action potential half-widths than PV cells from preadolescent mice (Doischer, Hosp et al. 2008, Okaty, Miller et al. 2009, Goldberg, Jeong et al. 2011, Miyamae, Chen et al. 2017). Moreover, PV cells from *Grin2a*$^{-/-}$ mice have a lower threshold to reach depolarization-induced block of

action potential firing and lower peak action potential firing frequencies. These latter electrophysiological characteristics could lead to failure of circuit level inhibition as interneuron depolarization increases, consistent with a hyperexcitable phenotype.

The exact mechanism for this transcriptional shift from immature to mature PV electrophysiological properties is not fully understood but has been shown to be activity-dependent (Miller, Okaty et al. 2011, Dehorter, Ciceri et al. 2015). Thus, the loss of *Grin2a* in developing PV interneurons appears to slow cellular maturation, potentially stemming from a loss of GluN2A signaling on PV cell dendrites or changes in non-cell autonomous signaling. All these properties ultimately reach WT levels in adult mice, suggesting that although GluN2A signaling may be sufficient to initiate these maturation transcriptional programs, it is not required. While the overall effects of a prolonged immature electrophysiological profile in preadolescent PV cells are not known, this period coincides with critical period plasticity in various brain regions (Hensch 2005, Takesian and Hensch 2013), and thus, could critically alter circuit formation in the hippocampus, and other regions. Specifically, larger input resistances and lower peak action potential firing frequencies will likely dampen the temporal resolution of inhibitory tone in a developing network, which may promote maladaptive plasticity and incorrect circuit wiring. Additionally, changes in depolarization-induced block of action potentials correlates with neural excitability and propagation of epileptiform activity (Calin, Ilie et al. 2021). Thus, disruption of PV cell function during development could have profound consequences for eventual mature networks that arise.

Methods

Animals and Breeding

All procedures involving the use of animals performed at Emory University were reviewed and approved by IACUC, and were performed in full accordance with state and federal Animal Welfare Acts and Public Health Service policies. *Grin2a*$^{-/-}$ mice were obtained from the laboratory of Masayoshi Mishina (University of Tokyo, Japan) and were generated via insertion of a neomycin resistance gene and Pau sequence (mRNA destabilizing and transcription-pausing signals) into the coding region of the transmembrane domain of the *Grin2a* gene as previously described (Sakimura, Kutsuwada et al. 1995). These mice were then backcrossed more than 15 times to a C57BL/6J (Jax stock number: 00664) background at Emory before use.

Mice were genotyped by performing PCRs for the neomycin cassette (forward: GGGCGCCCGGTTCTT; reverse: CCTCGTCCTGCAGTTCATTCA) and the WT *Grin2a* gene (forward: GCCCGTCCAGAATCCTAAAGG; reverse: GCAAAGAAGGCCCACACTGATA). In order to visualize PV cells for use in electrophysiological experiments, *Grin2a*$^{+/+}$ and *Grin2a*$^{-/-}$ mice were crossed with PV-TdTom mice (Jax stock number: 027395, Tg(Pvalb-tdTomato15Gfng)) to generate PV-TdTom:*Grin2a*$^{+/+}$ and PV-TdTom:*Grin2a*$^{-/-}$ mice. This reporter line has already been backcrossed to a C57BL/6J background and has been previously validated to be selective and specific for PV^{+}-GABAergic interneurons, including those within the CA1 subfield (Kaiser, Ting et al. 2016, Ekins, Mahadevan et al. 2020).

All mice were maintained in a conventional vivarium, given standard chow and water *ad libitum*, with a 12-hour light cycle. Both male and female mice were used in all experiments.

Seizure Induction Experiments

All seizure induction experiments were performed as previously described, using neonatal (P12-15) and adult (P70-130) *Grin2a*$^{+/+}$ and *Grin2a*$^{-/-}$ mice (Eun, Abraham et al. 2015, Shapiro, Gado et al. 2021). Experimenter was blinded to genotype during all experiments.

For lipopolysaccharide and febrile-induced seizures, neonatal mice were subjected to 0.1 mg/kg intraperitoneal lipopolysaccharide (E. coli strain O111:B4; Sigma, L2630) injection and returned to their home cage for 2 hours. After incubation, rectal temperatures were obtained before individual mice were placed in a plexiglass chamber (13 × 24 × 12.6 cm) and heated by a heat lamp positioned approximately 10 cm above the chamber. Baseline temperature was elevated by 0.5°C every 2 minutes until a seizure occurred or until temperature exceeded 42.5°C. If temperature did exceed 42.5°C, mice were removed from the heating chamber and allowed to cool for 3-5 minutes before being placed back in the chamber for continued heating. The experiment ended once 30 minutes of hyperthermia had elapsed or if mice displayed a generalized tonic-clonic seizure. Following 30 minutes of hyperthermia, animals were cooled on a metal surface, rehydrated by saline injection, and returned to their dams.

For pentylenetetrazol (PTZ)-induced seizures, adult mice were administered a single subcutaneous injection of PTZ (100 mg/kg) dissolved in 0.9%. saline (Sigma-Aldrich, P6500) and monitored for the occurrence of the first generalized tonic-clonic seizures over a 30-minute observation period. If mice did not seizure after 30 minutes, the experiment was ended by isoflurane overdose and mice recorded a time value of 1,800 seconds. For flurothyl-induced seizures, adult mice were placed in a plexiglass chamber (13.5 x 8 x 6 in.) and exposed to the inhaled chemoconvulsant flurothyl (bis[2,2,2-trifluoroethyl] ether, Sigma-Aldrich, 287571), at a flow rate of 20 µL/min. The latency to the first generalized tonic-clonic seizure was recorded. For 6 Hz induced seizures, adult mice were administered the topical anesthetic proparacaine hydrochloride ophthalmic solution (Patterson Veterinary, 07-885-9765), in each eye 5 minutes prior to seizure induction. Mice were then subjected to a corneal electrostimulation

(6 Hz, 2 ms pulse width, 3 sec duration) at 24 mA using an electroconvulsive therapy unit (Ugo Basile). Behavioral seizures were scored using a modified Racine scale: 0, no seizure; 1, staring/immobile for > 3 seconds; 2, forelimb clonus; 3, rearing and falling.

Immunohistochemistry for GABAergic Interneuron Markers

After mice were overdosed with inhaled isoflurane, they were transcardially perfused with cold 1x phosphate buffered saline (PBS; pH 7.35), and subsequently perfused with cold 4% paraformaldehyde (PFA) in 1x PBS. Brains were removed and fixed for 24 hours in 4% PFA in 1X PBS before being transferred to a 30% sucrose solution dissolved in 1x PBS until the brains sank. After cryoprotection, brains were frozen in optimal cutting temperature solution (OCT, Fisher) and serial 50-µm coronal hippocampal sections were obtained, with a total of five sections per animal, spaced roughly 250-µm apart. Slices were then transferred to a permeabilization solution containing 1.2% Triton-X in 1x PBS for 10 minutes, as previously described (Kaiser, Ting et al. 2016), before they were incubated in blocking solution containing 15% normal goat serum, 1% bovine serum albumin, and 0.5% Triton-X for two-four hours at room temperature. Primary antibodies were diluted in this same blocking solution at the following concentrations and incubated at 4°C for 72 hours: rabbit anti-parvalbumin (Swant, PV27; 1:5000) and rabbit anti-prepro-cholecystokinin (Frontier Institute Co., Ab-Rf350; 1:1000). After primary incubation, slices were washed 3 times in 1x PBS for 10 minutes then incubated in blocking solution containing AlexaFlour488 conjugated second antibodies (Abcam, ab150077; 1:1000) for 2-4 hours at room temperature. Slices were then washed 3 times in 1x PBS for 10 minutes then incubated in DAPI counterstain (Abcam, ab228549; 2 µM) for 30 minutes before being washed 3 more times in 1x PBS for 10 minutes. Slices were mounted on Superfrost Plus slides (Fisher Scientific, 12-550-15) and coverslipped with #1.5 coverslips (Thomas Scientific, 64-0717) using ProLong Gold Antifade mounting media (ThermoFisher, P36930). After mounting media had cured, slides were sealed with CoverGrip (Biotium, 23005).

Immunohistochemistry for GABAergic Synaptic Puncta

Double immunofluorescent staining for GABAergic synaptic puncta was performed as previously described (McLeod, Marzo et al. 2017). After mice were overdosed with inhaled isoflurane, brains were rapidly removed and 200-µm thick horizontal hippocampal slices were made using a vibratome (Leica, VT-1200S) in an ice-cold, sucrose-based artificial cerebrospinal fluid (aCSF) containing the following (in mM): 88 sucrose, 80 NaCl, 2.5 KCl, 1.25 HNa_2PO_4, 26 $HNaCO_3$, 10 glucose, 2 thiourea, 3 sodium pyruvate, 5 sodium ascorbate, 12 N-acetylcysteine, 10 $MgSO_4$, and 0.5 $CaCl_2$ bubbled in 95% O_2/5% CO_2. After sectioning, slices were incubated in a sucrose-based aCSF as described above but with 4 mM $MgSO_4$ at 32°C for 30 minutes before being returned to room temperature for an hour. Next, slices were incubated in 4% PFA in 1x PBS for 45 minutes before being washed 3 times in 1x PBS for 10 minutes. After fixation, individual slices were transferred to a single well in a 48-well plate to prevent slices from sticking together and sequentially stained using the methods outlined for immunohistochemistry above. Tissue was incubated with primary antibodies overnight at 4°C using the following concentrations: rabbit anti-gephyrin (Synaptic Systems, 147008; 1:500), guinea pig anti-vGAT (Synaptic Systems, 131013; 1:500), and mouse anti-synaptotagmin II (Abcam, ab154035; 1:500). After 3 washes in 1x PBS for 10 minutes each, tissue was incubated at room temperature for 2-4 hours using the following secondary antibodies: goat anti-rabbit Alexa488 (Abcam, ab150077; 1:1000), donkey anti-guinea pig Alexa647 (Jackson Immuno, 706-605-148; 1:1000), and donkey anti-mouse Alexa647 (Jackson Immuno, 715-605-151; 1:1000). After the doublestaining was complete, slices were counterstained with DAPI, mounted, coverslipped, and sealed as described above. A total 4-5 slices from 4 mice per genotype were used.

Image Acquisition and Analysis

All images were acquired using a Nikon A1R HD25 line-scanning confocal microscope using NIS Elements software. The following argon laser lines were used (in nm): 405, 488, and 647. The 405 and 488 nm laser line data were collected using GaAsP PMTs and the 647 nm laser line data was collected using a Multi-Alkali PMT. All images were a series of z-stacks captured using a piezo motor z-controller, with software set to acquire data in 1024 x 1024 pixel format at a 1/8th frame rate dwell time. One experimenter performed all analyses and was blinded to genotype during acquisition and counting of confocal microscopy data.

All GABAergic interneuron marker images were captured using Plan Apo 10x 0.45 NA objective, with some representative images captured using a Plan Apo 20x 0.75 NA objective, with images consisting of 11-14 stacks with a z-stack distance of 1 um and a pinhole size of 19.4 µm. 4-5 hippocampi from each animal were imaged across 4 animals per genotype. All images were analyzed in Imaris 9.5 (Bitplane) by manually drawing hippocampal subregion boundaries and hand-counted.

All GABAergic interneuron synaptic density images were captured using an Apo TIRF 60x 1.49 NA objective plus 3x additional zoom, with images consisting of 7-9 stacks with a z-stack distance of (0.1 µm) and a pinhole size of 30.4 µm. All images were analyzed in Imaris 9.5 (Bitplane) by implementing a 1-um radius background subtraction before using the 'Spots' feature to automatically label puncta. All puncta were set as being 0.3 µm. For gephyrin and SytII puncta, the threshold was set to 60% of the maximum reported value under the quality filter, and for vGAT puncta this was set to 50% of the maximum reported value under the quality filter. Next, spots were subjected to a distance-based colocalization algorithm (threshold at 0.6 or less, corresponding to a distance of roughly 300-400 nm), under 'Colocalize spots'. All data were normalized to the individual stack volume with data from 4-6 hippocampi per animal across 4 animals per genotype.

Acute Hippocampal Slice Preparation and Electrophysiological Recordings

After mice were overdosed with inhaled isoflurane, brains were rapidly removed and 300-µm thick horizontal hippocampal slices were made using a vibratome (Lecia, VT-1200S) in an ice-cold, sucrose-based aCSF solution as described above (See: Immunohistochemistry for GABAergic Synaptic Puncta). After sectioning, slices were incubated in a sucrose-based aCSF as described above but with 4 mM magnesium sulfate at 32°C for 30 minutes before being returned to room temperature for an hour before use.

All recordings were made in the following aCSF extracellular solution (in mM): 126 NaCl, 2.5 KCl, 1.25 HNa_2PO_4, 26 $HNaCO_3$, 20 glucose, 1.5 $MgSO_4$, and 1.5 $CaCl_2$ bubbled with 95% O_2/5% CO_2 and held at 30-32°C using an inline heater (Warner, SH-27B). Cells were visualized using an upright Olympus BX50W microscope with IR-DIC optics coupled to a Dage IR-2000 camera. Whole-cell patch clamp recordings were obtained using an Axopatch 200B (Molecular Devices) or a Multiclamp 700B (Molecular Devices, digitized at 20 kHz using an Digidata 1440a (Molecular Devices) and controlled by pClamp 10.6 software (Molecular Devices). All signals were low-pass filtered at 2 kHz using a Bessel 8-pole filter (Warner, LPF-8). Patch clamp electrodes were pulled using a Sutter P1000 horizontal puller from thin-walled borosilicate capillary tubes (WPI), with a typical resistance of 4-8 MΩ.

For mIPSCs the following intracellular solution was used (in mM): 135 cesium chloride, 3.5 NaCl, 1 $MgCl_2$, 10 HEPES, 0.6 EGTA, 2 Na_2ATP, 0.3 Na_2GTP, 5 sodium phosphocreatine, and 3 QX-314 . After obtaining a whole-cell configuration, cells were held at -60 mV to minimize depolarization-induced suppression of inhibition (Diana and Marty 2003) and were allowed to dialyze for ten minutes before NBQX (10 µM) and TTX (1 µM) were washed onto the slice for five minutes. mIPSCs recordings were made for a total for five minutes (with the last two minutes being used for analysis) before DAMGO (selective mu-opioid receptor agonist, 1 µM) was washed onto the slice, with the last two minutes being used for analysis. All recordings were finished in gabazine (10 µM). Data were analyzed offline using MiniAnalysis (Synaptosoft) with an 8-pA amplitude threshold for event detection. A weighted time constant

was calculated using the following formula by fitting a dual-exponential function to each composite mIPSC trace in ChanneLab (Synaptosoft):

(1) $\tau_W = (\tau_{FAST} (amplitude_{FAST} / (amplitude_{FAST} + amplitude_{SLOW}))) + (\tau_{SLOW} (amplitude_{SLOW} / (amplitude_{FAST} + amplitude_{SLOW})))$

For intrinsic and action potential firing properties of PV^+-cells, the following intracellular solution was used (in mM): 115 potassium gluconate, 0.6 EGTA, 2 $MgCl_2$, 2 Na_2ATP, 0.3 Na_2GTP, 10 HEPES, 5 sodium phosphocreatine, 8 KCl, and 0.3% biocytin. After obtaining a whole-cell configuration, cells were allowed to dialyze for 5 minutes in current-clamp mode at I=0. Liquid junction potential was not corrected for resting membrane potential and all current-clamp responses were automatically bridge-balanced using the Multiclamp 700B clamp commander software. Input resistance was calculated using the slope of voltage deflections in response to 500 ms current injections of -200, -150, -100, -50, 0, and 50 pA, with an inter-sweep interval of 2 seconds. The membrane time constant was calculated in response 20-30 sweeps of a 500 ms, -50 pA current injection, with an inter-sweep interval of 2 seconds. Composite responses were made by averaging 20-25 traces together using Clampfit (Molecular Devices). A weighted time constant was calculated using formula (1) by fitting a dual-exponential to each response in ChanneLab (Synaptosoft). Rheobase was calculated in response to 500 ms current injections starting at 0 pA and increasing by 2 pA every 2 seconds. Rheobase was defined as the minimal current injection required to elicit an action potential during the current injection period. Action potential firing frequency was calculated in response a 500 ms current injection every 2 seconds starting at -100 pA and increasing by 50 pA until the cell displayed depolarization-induced block of firing. Number of action potentials per current injection were calculated using MiniAnalysis (SynaptoSoft). Action potential half-width, action potential amplitude, action potential threshold, and afterhyperpolarization amplitude were calculated using the 'findpeaks' command in MATLAB, along with custom written scripts, from action potentials obtained during rheobase recordings.

Series resistance was monitored throughout all experiments and was typically 8−20 MΩ. For mIPSC experiments, a 5 mV square waveform (50 ms duration) was injected every 30 seconds during the recording epoch. For current clamp experiments, cells were briefly switched to voltage clamp and held at -60 mV while a series of 50 ms, 5 mV square waveforms were applied to the cell. mIPSC series resistance was monitored throughout the entire recording, while current clamp recordings had series resistance measurements made at the beginning and at the end of the entire experiment, which usually lasted 5-7 minutes total. All series resistances were measured offline by analyzing the peak of the capacitive charging spike and applying Ohm's law. If the series resistance changed >25% during the experiment, or ever exceeded 30 MΩ, then the cell was excluded.

Interneuron Anatomical Reconstructions

After biocytin filling during whole-cell recordings, slices were fixed with 4% PFA in 1x PBS overnight, then permeabilized with 0.3% Triton-X in 1x PBS and incubated with streptavidin Alexa555 (ThermoFisher, S21381; 1:1000). Resectioned slices (75-µm) were mounted on gelatin-coated slides using Mowiol mounting medium. Cells were visualized using epifluorescence microscopy and images for representative examples were obtained with confocal microscopy. Cells were reconstructed and analyzed with Sholl analysis using Neurolucida software (MBF Bioscience). Polar histograms of WT and *Grin2a*$^{-/-}$ dendrites and axons were created using the Neurolucida function (10 degree bins). Polarity preference was determined by calculating the percentage of horizontally (150–210, 330–30 degrees) or vertically (60–120, 240–300 degrees) oriented axons for each genotype.

Statistical Analysis and Figure Preparation

The two-sample, two-tailed Student's *t*-test was used for interneuron density counts, synaptic colocalization, and *in vitro* electrophysiology. The Kolmogorov-Smirnov test was used for *in vitro* electrophysiology data where cumulative distributions were being compared. For induced seizures experiments the chi-squared test, Mantel-Cox log-rank test, or Mann-Whitney rank-sum test was used where appropriate. For experiments where multiple statistical analyses were performed on the same dataset, our significance threshold was lowered to correct for family-wise error rate (FWER) using the Bonferroni post-hoc correction method. All studies were designed so that an effect size of at least 1 was detected at 80% or greater power.

Acknowledgements and Disclosures

Research reported in this publication was supported in part by an Emory University Synergy grant awarded to S.K. and S.F.T. as well as by the Emory University Integrated Cellular Imaging Core and Children's Healthcare of Atlanta. This work was supported by the following grants from the National Institutes of Health, National Institute of Neurological Disease and Stroke: NS113530 (C.R.C.), MH127404 (H.Y.), HD082373 (H.Y.), and NS111619 (S.F.T.). The content is solely the responsibility of the authors and does not necessarily reflect the official views of the National Institute of Health. The authors would also like to thank Steven Hunt and Andrew Hancock for their assistance with interneuron morphological analysis, and Nicholas Varvel and Asheebo Rojas for their assistance with general immunohistochemistry.

H.Y. and S.F.T. are co-inventors of Emory-owned intellectual property. S.F.T. is a PI on a research grants from Biogen, and Janssen to Emory, is a member of the SAB for Sage Therapeutics, Eumentis Therapeutics, the GRIN2B Foundation, and the CureGRIN Foundation. H.Y. is the PI on a research grant from Sage Therapeutics to Emory. S.F.T. owns stock in a company (NeurOp, Inc.) that is developing a GluN2B antagonist.

References

Acutain, M. F., J. Griebler Luft, C. A. Vazquez, B. Popik, M. C. Cercato, A. Epstein, A. Salvetti, D. A. Jerusalinsky, L. de Oliveira Alvares and M. V. Baez (2021). "Reduced Expression of Hippocampal GluN2A-NMDAR Increases Seizure Susceptibility and Causes Deficits in Contextual Memory." Front Neurosci **15**: 644100.

Adesnik, H., G. Li, M. J. During, S. J. Pleasure and R. A. Nicoll (2008). "NMDA receptors inhibit synapse unsilencing during brain development." Proc Natl Acad Sci U S A **105**(14): 5597-5602.

Akazawa, C., R. Shigemoto, Y. Bessho, S. Nakanishi and N. Mizuno (1994). "Differential expression of five N-methyl-D-aspartate receptor subunit mRNAs in the cerebellum of developing and adult rats." J Comp Neurol **347**(1): 150-160.

Akgul, G., D. Abebe, X. Q. Yuan, K. Auville and C. J. McBain (2019). "The Role of AMPARs in the Maturation and Integration of Caudal Ganglionic Eminence-Derived Interneurons into Developing Hippocampal Microcircuits." Sci Rep **9**(1): 5435.

Amador, A., C. D. Bostick, H. Olson, J. Peters, C. R. Camp, D. Krizay, W. Chen, W. Han, W. Tang, A. Kanber, S. Kim, J. Teoh, M. Sah, S. Petri, H. Paek, A. Kim, C. M. Lutz, M. Yang, S. J. Myers, S. Bhattacharya, H. Yuan, D. B. Goldstein, A. Poduri, M. J. Boland, S. F. Traynelis and W. N. Frankel (2020). "Modelling and treating GRIN2A developmental and epileptic encephalopathy in mice." Brain **143**(7): 2039-2057.

Amin, J. B., G. R. Moody and L. P. Wollmuth (2021). "From bedside-to-bench: What disease-associated variants are teaching us about the NMDA receptor." J Physiol **599**(2): 397-416.

Bard, L. and L. Groc (2011). "Glutamate receptor dynamics and protein interaction: lessons from the NMDA receptor." Mol Cell Neurosci **48**(4): 298-307.

Barria, A. and R. Malinow (2002). "Subunit-specific NMDA receptor trafficking to synapses." Neuron **35**(2): 345-353.

Benke, T. A., K. Park, I. Krey, C. R. Camp, R. Song, A. J. Ramsey, H. Yuan, S. F. Traynelis and J. Lemke (2021). "Clinical and therapeutic significance of genetic variation in the GRIN gene family encoding NMDARs." Neuropharmacology **199**: 108805.

Booker, S. A., A. Sumera, P. C. Kind and D. J. A. Wyllie (2021). "Contribution of NMDA Receptors to Synaptic Function in Rat Hippocampal Interneurons." eNeuro **8**(4).

Bortone, D. and F. Polleux (2009). "KCC2 expression promotes the termination of cortical interneuron migration in a voltage-sensitive calcium-dependent manner." Neuron **62**(1): 53-71.

Boyce-Rustay, J. M. and A. Holmes (2006). "Genetic inactivation of the NMDA receptor NR2A subunit has anxiolytic- and antidepressant-like effects in mice." Neuropsychopharmacology **31**(11): 2405-2414.

Butt, S. J., V. H. Sousa, M. V. Fuccillo, J. Hjerling-Leffler, G. Miyoshi, S. Kimura and G. Fishell (2008). "The requirement of Nkx2-1 in the temporal specification of cortical interneuron subtypes." Neuron **59**(5): 722-732.

Calin, A., A. S. Ilie and C. J. Akerman (2021). "Disrupting epileptiform activity by preventing parvalbumin interneuron depolarization block." J Neurosci.

Carvill, G. L., B. M. Regan, S. C. Yendle, B. J. O'Roak, N. Lozovaya, N. Bruneau, N. Burnashev, A. Khan, J. Cook, E. Geraghty, L. G. Sadleir, S. J. Turner, M. H. Tsai, R. Webster, R. Ouvrier, J. A. Damiano, S. F. Berkovic, J. Shendure, M. S. Hildebrand, P. Szepetowski, I. E. Scheffer and H. C. Mefford (2013). "GRIN2A mutations cause epilepsy-aphasia spectrum disorders." Nat Genet **45**(9): 1073-1076.

Chittajallu, R., J. C. Wester, M. T. Craig, E. Barksdale, X. Q. Yuan, G. Akgul, C. Fang, D. Collins, S. Hunt, K. A. Pelkey and C. J. McBain (2017). "Afferent specific role of NMDA receptors for the circuit integration of hippocampal neurogliaform cells." Nat Commun **8**(1): 152.

Collingridge, G. (1987). "Synaptic plasticity. The role of NMDA receptors in learning and memory." Nature **330**(6149): 604-605.

Crone, N. E., A. Sinai and A. Korzeniewska (2006). "High-frequency gamma oscillations and human brain mapping with electrocorticography." Prog Brain Res **159**: 275-295.

De Felipe, J., P. Marco, A. Fairen and E. G. Jones (1997). "Inhibitory synaptogenesis in mouse somatosensory cortex." Cereb Cortex **7**(7): 619-634.

De Marco Garcia, N. V., R. Priya, S. N. Tuncdemir, G. Fishell and T. Karayannis (2015). "Sensory inputs control the integration of neurogliaform interneurons into cortical circuits." Nat Neurosci **18**(3): 393-401.

Dehorter, N., G. Ciceri, G. Bartolini, L. Lim, I. del Pino and O. Marin (2015). "Tuning of fast-spiking interneuron properties by an activity-dependent transcriptional switch." Science **349**(6253): 1216-1220.

Denaxa, M., G. Neves, A. Rabinowitz, S. Kemlo, P. Liodis, J. Burrone and V. Pachnis (2018). "Modulation of Apoptosis Controls Inhibitory Interneuron Number in the Cortex." Cell Rep **22**(7): 1710-1721.

Diana, M. A. and A. Marty (2003). "Characterization of depolarization-induced suppression of inhibition using paired interneuron--Purkinje cell recordings." J Neurosci **23**(13): 5906-5918.
Doischer, D., J. A. Hosp, Y. Yanagawa, K. Obata, P. Jonas, I. Vida and M. Bartos (2008). "Postnatal differentiation of basket cells from slow to fast signaling devices." J Neurosci **28**(48): 12956-12968.
Drake, C. T. and T. A. Milner (2002). "Mu opioid receptors are in discrete hippocampal interneuron subpopulations." Hippocampus **12**(2): 119-136.
Dumas, T. C. (2005). "Developmental regulation of cognitive abilities: modified composition of a molecular switch turns on associative learning." Prog Neurobiol **76**(3): 189-211.
Ekins, T. G., V. Mahadevan, Y. Zhang, J. A. D'Amour, G. Akgul, T. J. Petros and C. J. McBain (2020). "Emergence of non-canonical parvalbumin-containing interneurons in hippocampus of a murine model of type I lissencephaly." Elife **9**.
Eun, B. L., J. Abraham, L. Mlsna, M. J. Kim and S. Koh (2015). "Lipopolysaccharide potentiates hyperthermia-induced seizures." Brain Behav **5**(8): e00348.
Evans, R. C., T. Morera-Herreras, Y. Cui, K. Du, T. Sheehan, J. H. Kotaleski, L. Venance and K. T. Blackwell (2012). "The effects of NMDA subunit composition on calcium influx and spike timing-dependent plasticity in striatal medium spiny neurons." PLoS Comput Biol **8**(4): e1002493.
Farrant, M. and Z. Nusser (2005). "Variations on an inhibitory theme: phasic and tonic activation of GABA(A) receptors." Nat Rev Neurosci **6**(3): 215-229.
Garcia-Junco-Clemente, P., G. Cantero, L. Gomez-Sanchez, P. Linares-Clemente, J. A. Martinez-Lopez, R. Lujan and R. Fernandez-Chacon (2010). "Cysteine string protein-alpha prevents activity-dependent degeneration in GABAergic synapses." J Neurosci **30**(21): 7377-7391.
Garcia-Recio, A., A. Santos-Gomez, D. Soto, N. Julia-Palacios, A. Garcia-Cazorla, X. Altafaj and M. Olivella (2021). "GRIN database: A unified and manually curated repertoire of GRIN variants." Hum Mutat **42**(1): 8-18.
Goldberg, E. M., H. Y. Jeong, I. Kruglikov, R. Tremblay, R. M. Lazarenko and B. Rudy (2011). "Rapid developmental maturation of neocortical FS cell intrinsic excitability." Cereb Cortex **21**(3): 666-682.
Goswami, S. P., I. Bucurenciu and P. Jonas (2012). "Miniature IPSCs in hippocampal granule cells are triggered by voltage-gated Ca2+ channels via microdomain coupling." J Neurosci **32**(41): 14294-14304.
Gray, J. A., Y. Shi, H. Usui, M. J. During, K. Sakimura and R. A. Nicoll (2011). "Distinct modes of AMPA receptor suppression at developing synapses by GluN2A and GluN2B: single-cell NMDA receptor subunit deletion in vivo." Neuron **71**(6): 1085-1101.
Hansen, K. B., L. P. Wollmuth, D. Bowie, H. Furukawa, F. S. Menniti, A. I. Sobolevsky, G. T. Swanson, S. A. Swanger, I. H. Greger, T. Nakagawa, C. J. McBain, V. Jayaraman, C. M. Low, M. L. Dell'Acqua, J. S. Diamond, C. R. Camp, R. E. Perszyk, H. Yuan and S. F. Traynelis (2021). "Structure, Function, and Pharmacology of Glutamate Receptor Ion Channels." Pharmacol Rev **73**(4): 298-487.
Hanson, E., M. Armbruster, L. A. Lau, M. E. Sommer, Z. J. Klaft, S. A. Swanger, S. F. Traynelis, S. J. Moss, F. Noubary, J. Chadchankar and C. G. Dulla (2019). "Tonic Activation of GluN2C/GluN2D-Containing NMDA Receptors by Ambient Glutamate Facilitates Cortical Interneuron Maturation." J Neurosci **39**(19): 3611-3626.
Hanson, J. E., M. Weber, W. J. Meilandt, T. Wu, T. Luu, L. Deng, M. Shamloo, M. Sheng, K. Scearce-Levie and Q. Zhou (2013). "GluN2B antagonism affects interneurons and leads to immediate and persistent changes in synaptic plasticity, oscillations, and behavior." Neuropsychopharmacology **38**(7): 1221-1233.
Hensch, T. K. (2005). "Critical period plasticity in local cortical circuits." Nat Rev Neurosci **6**(11): 877-888.
Hu, H., J. Gan and P. Jonas (2014). "Interneurons. Fast-spiking, parvalbumin(+) GABAergic interneurons: from cellular design to microcircuit function." Science **345**(6196): 1255263.
Inoue, M., M. Mishina and H. Ueda (2003). "Locus-specific rescue of GluRepsilon1 NMDA receptors in mutant mice identifies the brain regions important for morphine tolerance and dependence." J Neurosci **23**(16): 6529-6536.
Jiang, H., W. Jiang, J. Zou, B. Wang, M. Yu, Y. Pan, Y. Lin, Y. Mao and Y. Wang (2015). "The GluN2B subunit of N-methy-D-asparate receptor regulates the radial migration of cortical neurons in vivo." Brain Res **1610**: 20-32.
Kaiser, T., J. T. Ting, P. Monteiro and G. Feng (2016). "Transgenic labeling of parvalbumin-expressing neurons with tdTomato." Neuroscience **321**: 236-245.
Kannangara, T. S., C. A. Bostrom, A. Ratzlaff, L. Thompson, R. M. Cater, J. Gil-Mohapel and B. R. Christie (2014). "Deletion of the NMDA receptor GluN2A subunit significantly decreases dendritic growth in maturing dentate granule neurons." PLoS One **9**(8): e103155.

Kannangara, T. S., B. D. Eadie, C. A. Bostrom, K. Morch, P. S. Brocardo and B. R. Christie (2015). "GluN2A-/- Mice Lack Bidirectional Synaptic Plasticity in the Dentate Gyrus and Perform Poorly on Spatial Pattern Separation Tasks." Cereb Cortex **25**(8): 2102-2113.
Kelsch, W., Z. Li, S. Wieland, O. Senkov, A. Herb, C. Gongrich and H. Monyer (2014). "GluN2B-containing NMDA receptors promote glutamate synapse development in hippocampal interneurons." J Neurosci **34**(48): 16022-16030.
Komuro, H. and P. Rakic (1993). "Modulation of neuronal migration by NMDA receptors." Science **260**(5104): 95-97.
Lau, B. K., B. P. Ambrose, C. S. Thomas, M. Qiao and S. L. Borgland (2020). "Mu-Opioids Suppress GABAergic Synaptic Transmission onto Orbitofrontal Cortex Pyramidal Neurons with Subregional Selectivity." J Neurosci **40**(31): 5894-5907.
Lin, Y., B. L. Bloodgood, J. L. Hauser, A. D. Lapan, A. C. Koon, T. K. Kim, L. S. Hu, A. N. Malik and M. E. Greenberg (2008). "Activity-dependent regulation of inhibitory synapse development by Npas4." Nature **455**(7217): 1198-1204.
Mahadevan, V., A. Mitra, Y. Zhang, X. Yuan, A. Peltekian, R. Chittajallu, C. Esnault, D. Maric, C. Rhodes, K. A. Pelkey, R. Dale, T. J. Petros and C. J. McBain (2021). "NMDARs Drive the Expression of Neuropsychiatric Disorder Risk Genes Within GABAergic Interneuron Subtypes in the Juvenile Brain." Front Mol Neurosci **14**: 712609.
Marquardt, K., M. Saha, M. Mishina, J. W. Young and J. L. Brigman (2014). "Loss of GluN2A-containing NMDA receptors impairs extra-dimensional set-shifting." Genes Brain Behav **13**(7): 611-617.
Matta, J. A., K. A. Pelkey, M. T. Craig, R. Chittajallu, B. W. Jeffries and C. J. McBain (2013). "Developmental origin dictates interneuron AMPA and NMDA receptor subunit composition and plasticity." Nat Neurosci **16**(8): 1032-1041.
McLeod, F., A. Marzo, M. Podpolny, S. Galli and P. Salinas (2017). "Evaluation of Synapse Density in Hippocampal Rodent Brain Slices." J Vis Exp(128).
Micheva, K. D., M. Kiraly, M. M. Perez and D. V. Madison (2021). "Extensive Structural Remodeling of the Axonal Arbors of Parvalbumin Basket Cells during Development in Mouse Neocortex." J Neurosci.
Miller, M. N., B. W. Okaty, S. Kato and S. B. Nelson (2011). "Activity-dependent changes in the firing properties of neocortical fast-spiking interneurons in the absence of large changes in gene expression." Dev Neurobiol **71**(1): 62-70.
Miyamae, T., K. Chen, D. A. Lewis and G. Gonzalez-Burgos (2017). "Distinct Physiological Maturation of Parvalbumin-Positive Neuron Subtypes in Mouse Prefrontal Cortex." J Neurosci **37**(19): 4883-4902.
Miyamoto, Y., K. Yamada, T. Nagai, H. Mori, M. Mishina, H. Furukawa, Y. Noda and T. Nabeshima (2004). "Behavioural adaptations to addictive drugs in mice lacking the NMDA receptor epsilon1 subunit." Eur J Neurosci **19**(1): 151-158.
Monyer, H., N. Burnashev, D. J. Laurie, B. Sakmann and P. H. Seeburg (1994). "Developmental and regional expression in the rat brain and functional properties of four NMDA receptors." Neuron **12**(3): 529-540.
Mozhui, K., R. M. Karlsson, T. L. Kash, J. Ihne, M. Norcross, S. Patel, M. R. Farrell, E. E. Hill, C. Graybeal, K. P. Martin, M. Camp, P. J. Fitzgerald, D. C. Ciobanu, R. Sprengel, M. Mishina, C. L. Wellman, D. G. Winder, R. W. Williams and A. Holmes (2010). "Strain differences in stress responsivity are associated with divergent amygdala gene expression and glutamate-mediated neuronal excitability." J Neurosci **30**(15): 5357-5367.
Murthy, S., M. Niquille, N. Hurni, G. Limoni, S. Frazer, P. Chameau, J. A. van Hooft, T. Vitalis and A. Dayer (2014). "Serotonin receptor 3A controls interneuron migration into the neocortex." Nat Commun **5**: 5524.
Nakazawa, K., T. J. McHugh, M. A. Wilson and S. Tonegawa (2004). "NMDA receptors, place cells and hippocampal spatial memory." Nat Rev Neurosci **5**(5): 361-372.
Nash, J. E. and J. M. Brotchie (2000). "A common signaling pathway for striatal NMDA and adenosine A2a receptors: implications for the treatment of Parkinson's disease." J Neurosci **20**(20): 7782-7789.
Nelson, K. B. and J. H. Ellenberg (1976). "Predictors of epilepsy in children who have experienced febrile seizures." N Engl J Med **295**(19): 1029-1033.
Okaty, B. W., M. N. Miller, K. Sugino, C. M. Hempel and S. B. Nelson (2009). "Transcriptional and electrophysiological maturation of neocortical fast-spiking GABAergic interneurons." J Neurosci **29**(21): 7040-7052.
Onogi, T., M. Minami, Y. Katao, T. Nakagawa, Y. Aoki, T. Toya, S. Katsumata and M. Satoh (1995). "DAMGO, a mu-opioid receptor selective agonist, distinguishes between mu- and delta-opioid receptors around their first extracellular loops." FEBS Lett **357**(1): 93-97.
Owens, D. F., X. Liu and A. R. Kriegstein (1999). "Changing properties of GABA(A) receptor-mediated signaling during early neocortical development." J Neurophysiol **82**(2): 570-583.
Pafundo, D. E., T. Miyamae, D. A. Lewis and G. Gonzalez-Burgos (2018). "Presynaptic Effects of N-Methyl-D-Aspartate Receptors Enhance Parvalbumin Cell-Mediated Inhibition of Pyramidal Cells in Mouse Prefrontal Cortex." Biol Psychiatry **84**(6): 460-470.
Paoletti, P., C. Bellone and Q. Zhou (2013). "NMDA receptor subunit diversity: impact on receptor properties, synaptic plasticity and disease." Nat Rev Neurosci **14**(6): 383-400.

Pelkey, K. A., R. Chittajallu, M. T. Craig, L. Tricoire, J. C. Wester and C. J. McBain (2017). "Hippocampal GABAergic Inhibitory Interneurons." Physiol Rev **97**(4): 1619-1747.
Perszyk, R. E., J. O. DiRaddo, K. L. Strong, C. M. Low, K. K. Ogden, A. Khatri, G. A. Vargish, K. A. Pelkey, L. Tricoire, D. C. Liotta, Y. Smith, C. J. McBain and S. F. Traynelis (2016). "GluN2D-Containing N-methyl-d-Aspartate Receptors Mediate Synaptic Transmission in Hippocampal Interneurons and Regulate Interneuron Activity." Mol Pharmacol **90**(6): 689-702.
Perszyk, R. E., S. J. Myers, H. Yuan, A. J. Gibb, H. Furukawa, A. I. Sobolevsky and S. F. Traynelis (2020). "Hodgkin-Huxley-Katz Prize Lecture: Genetic and pharmacological control of glutamate receptor channel through a highly conserved gating motif." J Physiol **598**(15): 3071-3083.
Priya, R., M. F. Paredes, T. Karayannis, N. Yusuf, X. Liu, X. Jaglin, I. Graef, A. Alvarez-Buylla and G. Fishell (2018). "Activity Regulates Cell Death within Cortical Interneurons through a Calcineurin-Dependent Mechanism." Cell Rep **22**(7): 1695-1709.
Ropert, N., R. Miles and H. Korn (1990). "Characteristics of miniature inhibitory postsynaptic currents in CA1 pyramidal neurones of rat hippocampus." J Physiol **428**: 707-722.
Royer, S., B. V. Zemelman, A. Losonczy, J. Kim, F. Chance, J. C. Magee and G. Buzsaki (2012). "Control of timing, rate and bursts of hippocampal place cells by dendritic and somatic inhibition." Nat Neurosci **15**(5): 769-775.
Sakimura, K., T. Kutsuwada, I. Ito, T. Manabe, C. Takayama, E. Kushiya, T. Yagi, S. Aizawa, Y. Inoue, H. Sugiyama and et al. (1995). "Reduced hippocampal LTP and spatial learning in mice lacking NMDA receptor epsilon 1 subunit." Nature **373**(6510): 151-155.
Salmi, M., R. Bolbos, S. Bauer, M. Minlebaev, N. Burnashev and P. Szepetowski (2018). "Transient microstructural brain anomalies and epileptiform discharges in mice defective for epilepsy and language-related NMDA receptor subunit gene Grin2a." Epilepsia **59**(10): 1919-1930.
Salmi, M., F. Del Gallo, M. Minlebaev, A. Zakharov, V. Pauly, P. Perron, A. Pons-Bennaceur, S. Corby-Pellegrino, L. Aniksztejn, P. P. Lenck-Santini, J. Epsztein, R. Khazipov, N. Burnashev, G. Bertini and P. Szepetowski (2019). "Impaired vocal communication, sleep-related discharges, and transient alteration of slow-wave sleep in developing mice lacking the GluN2A subunit of N-methyl-d-aspartate receptors." Epilepsia **60**(7): 1424-1437.
Shao, C., P. Chen, Q. Chen, M. Zhao, W. N. Zhang and K. Yang (2020). "Mu opioid receptors inhibit GABA release from parvalbumin interneuron terminals onto CA1 pyramidal cells." Biochem Biophys Res Commun **522**(4): 1059-1062.
Shapiro, L., F. Gado, C. Manera and A. Escayg (2021). "Allosteric modulation of the cannabinoid 2 receptor confers seizure resistance in mice." Neuropharmacology **188**: 108448.
Sheng, M., J. Cummings, L. A. Roldan, Y. N. Jan and L. Y. Jan (1994). "Changing subunit composition of heteromeric NMDA receptors during development of rat cortex." Nature **368**(6467): 144-147.
Shipton, O. A. and O. Paulsen (2014). "GluN2A and GluN2B subunit-containing NMDA receptors in hippocampal plasticity." Philos Trans R Soc Lond B Biol Sci **369**(1633): 20130163.
Sohal, V. S., F. Zhang, O. Yizhar and K. Deisseroth (2009). "Parvalbumin neurons and gamma rhythms enhance cortical circuit performance." Nature **459**(7247): 698-702.
Soltesz, I., D. K. Smetters and I. Mody (1995). "Tonic inhibition originates from synapses close to the soma." Neuron **14**(6): 1273-1283.
Sommeijer, J. P. and C. N. Levelt (2012). "Synaptotagmin-2 is a reliable marker for parvalbumin positive inhibitory boutons in the mouse visual cortex." PLoS One **7**(4): e35323.
Southwell, D. G., M. F. Paredes, R. P. Galvao, D. L. Jones, R. C. Froemke, J. Y. Sebe, C. Alfaro-Cervello, Y. Tang, J. M. Garcia-Verdugo, J. L. Rubenstein, S. C. Baraban and A. Alvarez-Buylla (2012). "Intrinsically determined cell death of developing cortical interneurons." Nature **491**(7422): 109-113.
Sussel, L., O. Marin, S. Kimura and J. L. Rubenstein (1999). "Loss of Nkx2.1 homeobox gene function results in a ventral to dorsal molecular respecification within the basal telencephalon: evidence for a transformation of the pallidum into the striatum." Development **126**(15): 3359-3370.
Takesian, A. E. and T. K. Hensch (2013). "Balancing plasticity/stability across brain development." Prog Brain Res **207**: 3-34.
Tricoire, L., K. A. Pelkey, M. I. Daw, V. H. Sousa, G. Miyoshi, B. Jeffries, B. Cauli, G. Fishell and C. J. McBain (2010). "Common origins of hippocampal Ivy and nitric oxide synthase expressing neurogliaform cells." J Neurosci **30**(6): 2165-2176.
Tricoire, L., K. A. Pelkey, B. E. Erkkila, B. W. Jeffries, X. Yuan and C. J. McBain (2011). "A blueprint for the spatiotemporal origins of mouse hippocampal interneuron diversity." J Neurosci **31**(30): 10948-10970.

Tyzio, R., A. Represa, I. Jorquera, Y. Ben-Ari, H. Gozlan and L. Aniksztejn (1999). "The establishment of GABAergic and glutamatergic synapses on CA1 pyramidal neurons is sequential and correlates with the development of the apical dendrite." J Neurosci **19**(23): 10372-10382.
Ultanir, S. K., J. E. Kim, B. J. Hall, T. Deerinck, M. Ellisman and A. Ghosh (2007). "Regulation of spine morphology and spine density by NMDA receptor signaling in vivo." Proc Natl Acad Sci U S A **104**(49): 19553-19558.
Wang, C. C., R. G. Held, S. C. Chang, L. Yang, E. Delpire, A. Ghosh and B. J. Hall (2011). "A critical role for GluN2B-containing NMDA receptors in cortical development and function." Neuron **72**(5): 789-805.
Wang, X. J. (2002). "Probabilistic decision making by slow reverberation in cortical circuits." Neuron **36**(5): 955-968.
Watanabe, D., H. Inokawa, K. Hashimoto, N. Suzuki, M. Kano, R. Shigemoto, T. Hirano, K. Toyama, S. Kaneko, M. Yokoi, K. Moriyoshi, M. Suzuki, K. Kobayashi, T. Nagatsu, R. J. Kreitman, I. Pastan and S. Nakanishi (1998). "Ablation of cerebellar Golgi cells disrupts synaptic integration involving GABA inhibition and NMDA receptor activation in motor coordination." Cell **95**(1): 17-27.
Yamasaki, M., R. Okada, C. Takasaki, S. Toki, M. Fukaya, R. Natsume, K. Sakimura, M. Mishina, T. Shirakawa and M. Watanabe (2014). "Opposing role of NMDA receptor GluN2B and GluN2D in somatosensory development and maturation." J Neurosci **34**(35): 11534-11548.

Table 1. Interneuron density counts.

	Preadolescent				Adult			
	WT	2AKO	p-value	Significant?	WT	2AKO	p-value	Significant?
Hippocampal PV Cells								
CA1 density (# / mm^3)	4875 ± 162	6488 ± 276	0.00003	yes	4436 ± 326	6212 ± 505	0.006	yes
CA3 density (# / mm^3)	6750 ± 357	7998 ± 438	0.0378	no	6754 ± 306	7502 ± 539	0.235	no
Total density (# / mm^3)	5534 ± 176	6941 ± 277	0.00022	yes	5241 ± 279	6916 ± 554	0.0105	yes
s.o. density (% total)	42 ± 2.8	39 ± 2.3	0.46	no	39 ± 2.5	38 ± 2.4	0.786	no
s.p. density (% total)	51 ± 2.8	52 ± 2.3	0.67	no	44 ± 2.5	51 ± 2	0.0526	no
s.r. density (% total)	7.5 ± 1.5	9.4 ± 1.9	0.45	no	17 ± 2.5	12 ± 1.7	0.1144	no
s.l.m. density (% total)	0	0	--	--	0	0	--	--
Number slices used	17	20	--	--	19	19	--	--
Number animals used	4	4	--	--	4	4	--	--
Hippocampal CCK Cells								
CA1 density (# / mm^3)	4060 ± 210	4209 ± 314	0.686	no	4130 ± 202	3708 ± 178	0.1245	no
CA3 density (# / mm^3)	4510 ± 239	4789 ± 301	0.473	no	4936 ± 254	3810 ± 278	0.0055	yes
Total density (# / mm^3)	4192 ± 182	4372 ± 245	0.558	no	4417 ± 178	3745 ± 126	0.0034	yes
s.o. density (% total)	24 ± 2.4	27 ± 2.3	0.351	no	28 ± 2.4	22 ± 2.8	0.1345	no
s.p. density (% total)	11 ± 2.1	18 ± 2.5	0.0434	no	8.9 ± 1.5	9.1 ± 1.7	0.9608	no
s.r. density (% total)	47 ± 2.2	45 ± 2.8	0.5962	no	46 ± 2.3	56 ± 3.3	0.0217	no
s.l.m. density (% total)	17 ± 2.4	9.3 ± 1.7	0.013	no	18 ± 2	14 ± 1.8	0.2558	no
Number slices used	20	20	--	--	18	20	--	--
Number animals used	4	4	--	--	4	4	--	--
Cortical CCK Cells								
Total density ((# / mm^3) * 1000)	22.3 ± 1.1	24.5 ± 1.4	0.257	no	24.4 ± 0.8	25.7 ± 1.4	0.383	no
Number slices used	13	17	--	--	17	14	--	--
Number animals used	3	3	--	--	3	3	--	--

Table 2. Synaptic densities via colocalization.

	Preadolescent				Adult			
	WT	2AKO	p-value	Significant?	WT	2AKO	p-value	Significant?
vGAT-Geph Colocalization Pyramidale								
Coloc puncta (# / um^3)	0.06 ± 0.01	0.08 ± 0.01	0.0347	yes	0.11 ± 0.01	0.15 ± 0.01	0.0032	yes
vGAT puncta (# / um^3)	0.27 ± 0.01	0.3 ± 0.02	--	--	0.31 ± 0.02	0.34 ± 0.01	--	--
Geph puncta (# / um^3)	0.16 ± 0.01	0.22 ± 0.01	--	--	0.27 ± 0.02	0.31 ± 0.02	--	--
Number slices used	19	20	--	--	20	20	--	--
Number animals used	4	4	--	--	4	4	--	--
vGAT-Geph Colocalization Radiatum								
Coloc puncta (# / um^3)	0.1 ± 0.01	0.11 ± 0.01	0.214	no	0.13 ± 0.01	0.16 ± 0.01	0.0249	yes
vGAT puncta (# / um^3)	0.27 ± 0.01	0.28 ± 0.01	--	--	0.24 ± 0.02	0.32 ± 0.01	--	--
Geph puncta (# / um^3)	0.37 ± 0.02	0.39 ± 0.02	--	--	0.44 ± 0.02	0.43 ± 0.04	--	--
Number slices used	19	20	--	--	20	20	--	--
Number animals used	4	4	--	--	4	4	--	--
SytII-Geph Colocalization Pyramidale								
Coloc puncta (# / um^3)	0.02 ± 0.01	0.03 ± 0.01	0.18	no	0.08 ± 0.01	0.12 ± 0.01	0.0028	yes
SytII puncta (# / um^3)	0.08 ± 0.02	0.13 ± 0.02	--	--	0.23 ± 0.01	0.26 ± 0.02	--	--
Geph puncta (# / um^3)	0.22 ± 0.01	0.26 ± 0.01	--	--	0.3 ± 0.02	0.37 ± 0.05	--	--
Number slices used	20	18	--	--	20	20	--	--
Number animals used	4	4	--	--	4	4	--	--
SytII-Geph Colocalization Radiatum								
Coloc puncta (# / um^3)	0.05 ± 0.01	0.04 ± 0.01	0.104	no	0.06 ± 0.01	0.09 ± 0.01	0.0094	yes
SytII puncta (# / um^3)	0.14 ± 0.01	0.13 ± 0.01	--	--	0.14 ± 0.01	0.16 ± 0.01	--	--
Geph puncta (# / um^3)	0.45 ± 0.03	0.39 ± 0.02	--	--	0.47 ± 0.03	0.55 ± 0.03	--	--
Number slices used	20	18	--	--	20	20	--	--
Number animals used	4	4	--	--	4	4	--	--

Table 3. Morphological analysis of preadolescent CA1 PV cells.

	Dendrites				Axons			
	WT	2AKO	p-value	Significant?	WT	2AKO	p-value	Significant?
Total length (µm * 100)	30.9 ± 4.3	28.7 ± 4.3	0.73	no	91.1 ± 12.3	82.6 ± 12.2	0.63	no
Sholl intersections	126 ± 17	118 ± 17	0.75	no	296 ± 41	274 ± 43	0.72	no
Age (postnatal days)	22 ± 0.4	22 ± 0.3	--	--	22 ± 0.4	22 ± 0.3	--	--
Number of cells	11	11	--	--	9	11	--	--
Number of animals	4	4	--	--	4	4	--	--

Table 4. Phasic inhibition and DAMGO application.

	Preadolescent				Adult			
	WT	2AKO	p-value	Significant?	WT	2AKO	p-value	Significant?
mIPSC Characteristics								
Frequency (Hz)	14.8 ± 1.9	12.9 ± 1.3	0.46	no	8 ± 0.76	9.3 ± 1.2	0.36	no
Amplitude (pA)	-32.5 ± 2.4	-28.9 ± 2.5	0.24	no	-28 ± 1.6	-28.4 ± 2	0.12	no
Decay time (ms)	12.3 ± 0.8	13.2 ± 0.8	0.42	no	13.5 ± 0.6	13.1 ± 0.9	0.68	no
mIPSC After DAMGO Application								
Frequency (% baseline)	-51 ± 3.7	-47.5 ± 3.5	0.49	no	-54.7 ± 2.5	-49.1 ± 2.7	0.14	no
Amplitude (% baseline)	-10.9 ± 3.3	-7.7 ± 3.9	0.54	no	-7.1 ± 4.1	-5.4 ± 4.1	0.77	no
Other Properties of Interest								
Series resistance (MΩ)	19.1 ± 0.7	19.4 ± 0.7	--	--	20.9 ± 0.9	16.8 ± 1	--	--
Age (postnatal days)	22 ± 0.5	23 ± 0.6	--	--	96 ± 6	104 ± 5	--	--
Number of cells	15	18	--	--	17	15	--	--
Number of animals	6	9	--	--	8	6	--	--

Table 5. Interneuron passive properties and action-potential firing characteristics.

	Preadolescent				Adult			
	WT	2AKO	p-value	Significant?	WT	2AKO	p-value	Significant?
Intrinsic Electrical Properties								
Resting potential (mV)	-65.4 ± 1.2	-63.3 ± 1.6	0.28	no	-62.4 ± 1.8	-62.5 ± 1.8	0.98	no
Capacitance (pF)	120.7 ± 6.7	117.1 ± 8.2	0.73	no	126.9 ± 13	117.3 ± 9.3	0.54	no
Input resistance (MΩ)	96.0 ± 7.9	148.5 ± 16	0.0032	yes	101.4 ± 9.7	107.1 ± 12	0.72	no
Time constant (ms)	11.1 ± 0.9	16.9 ± 1.9	0.0058	yes	11.8 ± 0.8	11.5 ± 0.8	0.78	no
Action Potential Characteristics								
Rheobase (pA)	133.3 ± 20	93.1 ± 19	0.15	no	128.3 ± 21	130 ± 19	0.95	no
AP half-width (ms)	0.49 ± 0.01	0.65 ± 0.05	0.0018	yes	0.53 ± 0.01	0.51 ± 0.03	0.74	no
AP amplitude (mV)	47.19 ± 1.1	47.5 ± 1.9	--	not tested	40.4 ± 2.4	44.2 ± 2.6	--	not tested
AP threshold (mV)	-45.6 ± 1.2	-46.9 ± 1.5	--	not tested	-44.3 ± 1.8	-42.4 ± 2.1	--	not tested
AHP amplitude (mV)	-12.8 ± 0.8	-12.7 ± 0.6	--	not tested	-10.6 ± 1.1	-10.1 ± 1.1	--	not tested
Max AP firing (Hz)	267.8 ± 13	186.4 ± 15	0.0002	yes	246.6 ± 16	250 ± 22	0.73	no
Max dV/dt at max fire	186 ± 5.6	161 ± 9.2	--	not tested	130 ± 11.8	147 ± 15.2	--	not tested
DIB (pA)	1374 ± 98	761 ± 106	0.0001	yes	1150 ± 161	1161 ± 170	0.96	no
Other Properties of Interest								
Series resistance (MΩ)	18.6 ± 0.6	19.2 ± 0.8	--	--	17.1 ± 0.6	17.2 ± 1.0	--	--
Age (postnatal days)	22 ± 0.4	22 ± 0.3	--	--	72 ± 2	78 ± 3	--	--
Number of cells	21	18	--	--	12	14	--	--
Number animals used	6	8	--	--	5	6	--	--

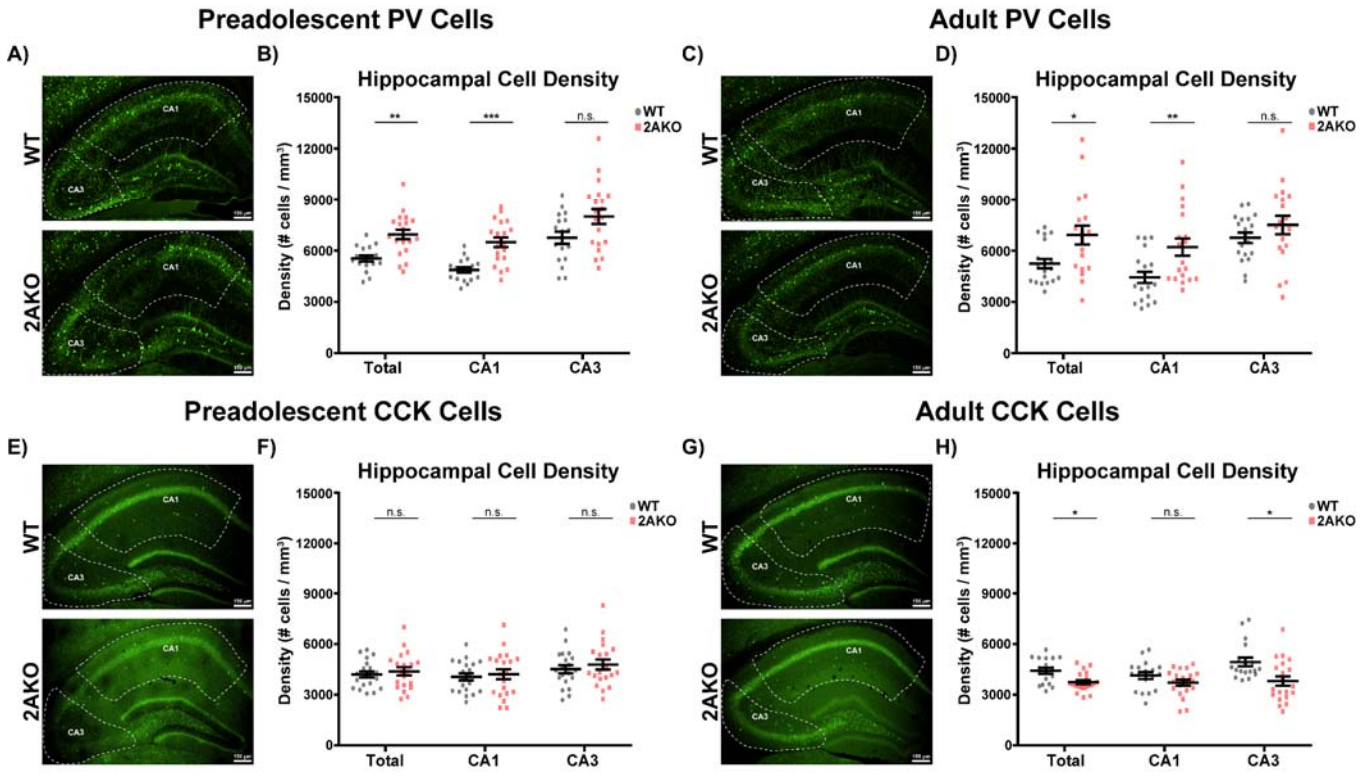

Figure 1. Loss of *Grin2a* causes an increase in parvalbumin (PV), but not cholecystokinin (CCK), cell density in CA1. Representative images of hippocampal sections stained for PV in A) preadolescent and C) adult WT and *Grin2a*$^{-/-}$ mice. PV cell density is significantly increased in CA1 in both B) preadolescent (4,875 ± 162 WT vs 6,488 ± 276 *Grin2a*$^{-/-}$ cells per mm^3; Student's two-sample t-test, p=0.00003) and D) adult (4,436 ± 326 WT vs 6,212 ± 505 *Grin2a*$^{-/-}$ cells per mm^3; Student's two-sample t-test, p=0.0055) mice. PV cell density is unchanged in CA3 in both preadolescent and adult mice. Representative images of hippocampal sections stained for CCK in E) preadolescent and G) adult WT and *Grin2a*$^{-/-}$ mice. There is no change in CA1 CCK cell density in either F) preadolescent or H) adult mice, however, there is a decrease in CA3 CCK cell density in adult *Grin2a*$^{-/-}$ mice (4,936 ± 254 WT vs 3,810 ± 278 *Grin2a*$^{-/-}$ cells per mm^3; Student's two-sample t-test, p=0.0055). Data obtained from 4-6 slices per animal with 4 animals used per genotype at each age. Symbols are mean ± SEM. WT = wildtype; 2AKO = *Grin2a*$^{-/-}$. * = p<0.05; ** = p<0.01; *** = p<0.001; n.s. = not significant.

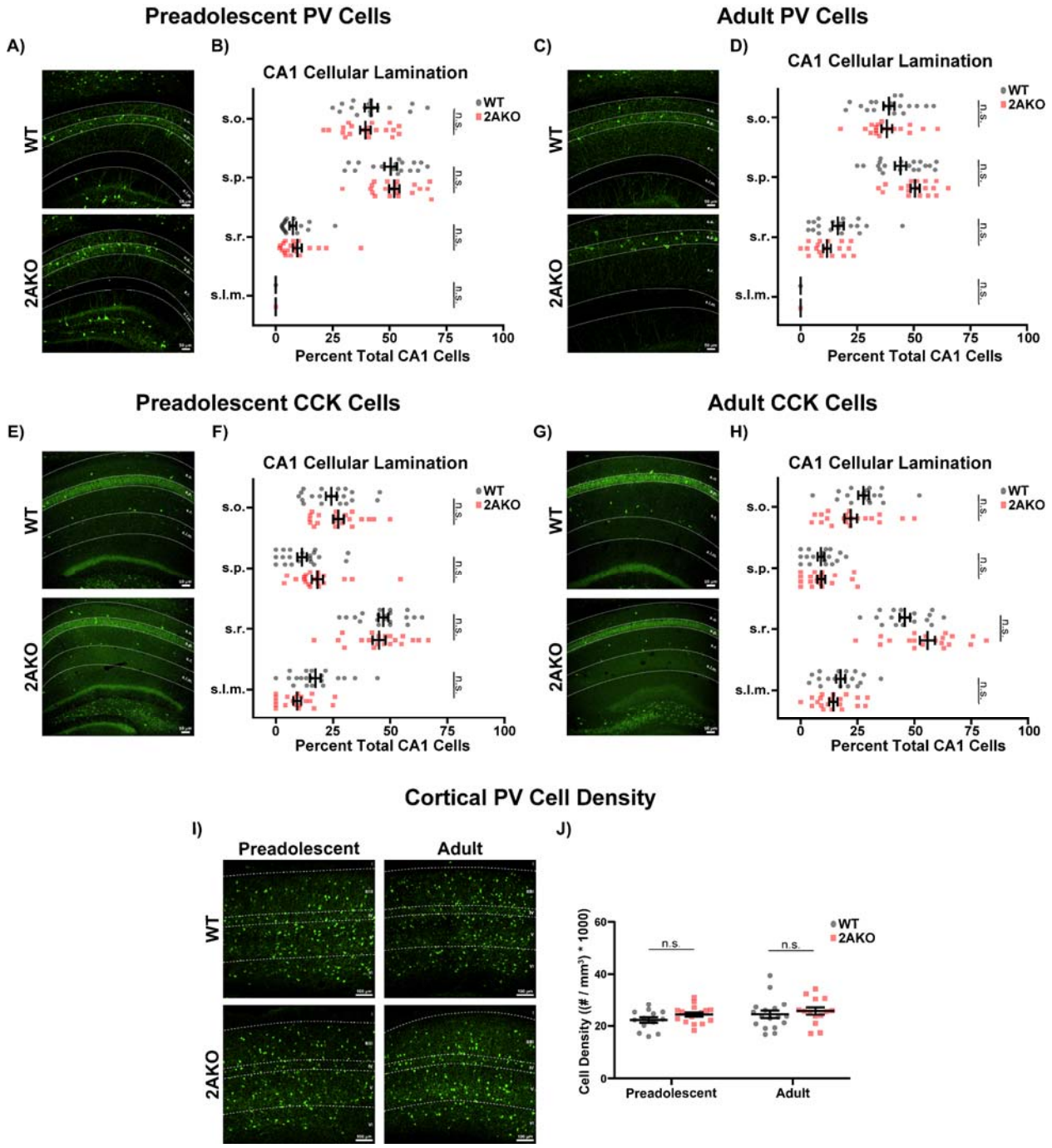

Supplemental Figure 1. Loss of *Grin2a* does not change parvalbumin (PV) or cholecystokinin (CCK) CA1 cellular lamination patterns or change cortical PV cell density. Representative images of the hippocampal CA1 subfield stained for PV in A) preadolescent and C) adult WT and *Grin2a*$^{-/-}$ mice. There is no change in CA1 PV cellular lamination in either B) preadolescent or D) adult *Grin2a*$^{-/-}$ mice. Representative images of hippocampal CA1 stained for CCK in E) preadolescent and F) adult WT and *Grin2a*$^{-/-}$ mice. There is no change in CA1 CCK cellular lamination in either B) preadolescent or D) adult *Grin2a*$^{-/-}$ mice. I) Representative images of the somatosensory cortex stained for PV in preadolescent and adult mice. J) There is no change in cortical PV cell density at either age between WT and *Grin2a*$^{-/-}$ mice. Data obtained from 4-6 slices per animal with 4 animals used per genotype at each age. Symbols are mean ± SEM. WT = wildtype; 2AKO = *Grin2a*$^{-/-}$. s.o. = *stratum oriens*; s.p. = *stratum pyramidale*; s.r. = *stratum radiatum*; s.l.m. = *stratum lucinosum moleculare*. n.s. = not significant.

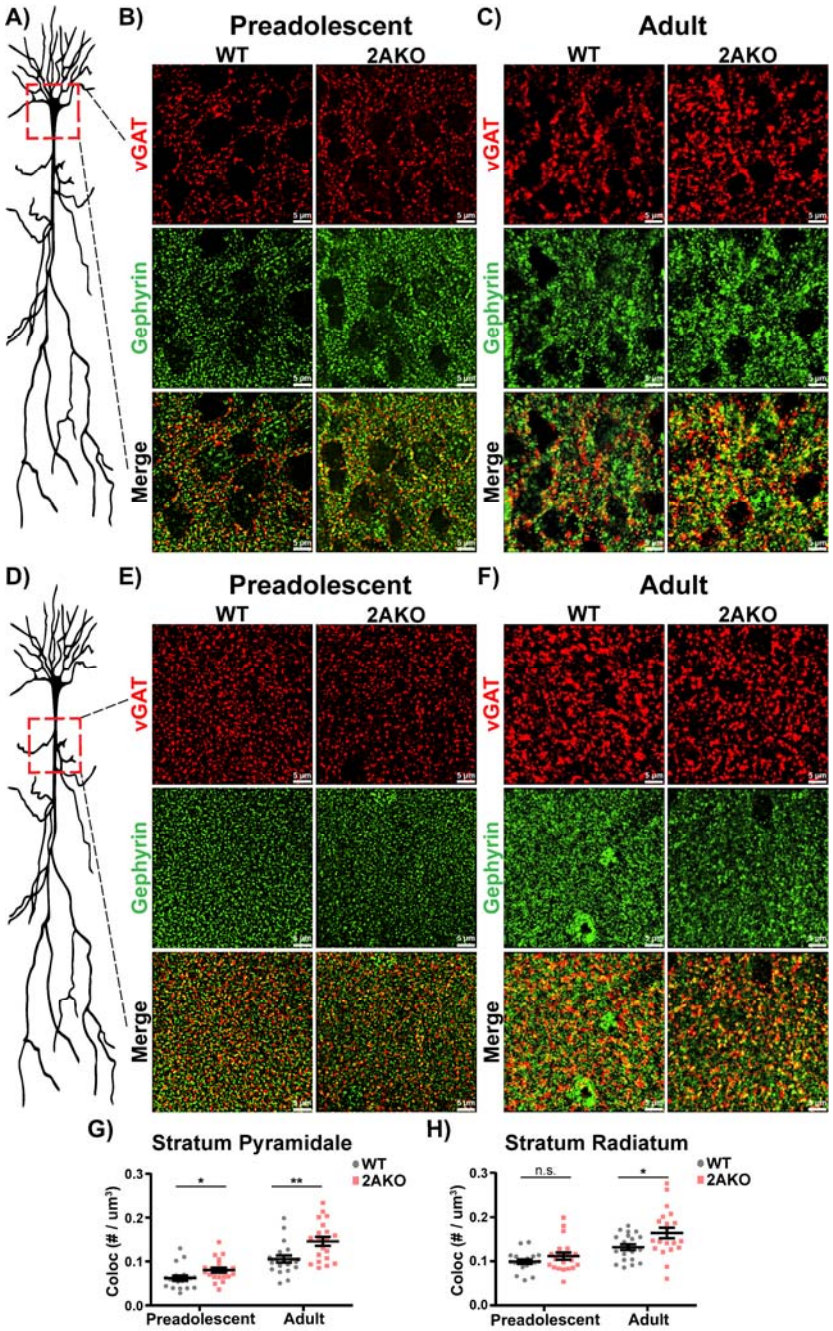

Figure 2. Loss of *Grin2a* causes an age-dependent increase in GABAergic synaptic density in the *stratum pyramidale* and *stratum radiatum* layers of CA1. Model pyramidal cell showing that images were captured in the A) *stratum pyramidale* or D) *stratum radiatum* layer of CA1. Representative images of sections stained for vGAT (presynaptic) and gephyrin (postsynaptic) GABAergic synaptic markers in the B) preadolescent *stratum pyramidale,* C) adult *stratum pyramidale*, E) preadolescent *stratum radiatum*, and F) adult *stratum radiatum* layers of CA1 in both wild type and *Grin2a*$^{-/-}$ mice. Synaptic density is defined as the colocalization of vGAT and gephyrin synaptic markers. G) In the *stratum pyramidale* and H) the *stratum radiatum*, there is an age-dependent increase of GABAergic synaptic density in *Grin2a*$^{-/-}$ mice. See Table 2 for individual values. Data obtained from 4-5 slices per animal with 4 animals used per genotype at each age. Symbols are mean ± SEM. WT = wildtype; 2AKO = *Grin2a*$^{-/-}$. Geph = gephyrin; coloc = vGAT/gephyrin colocalized puncta. * = $p<0.05$; ** = $p<0.01$; n.s. = not significant.

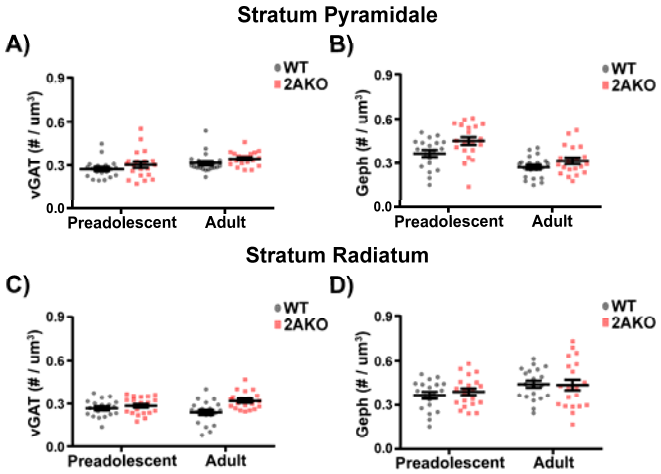

Supplemental Figure 2. Individual puncta numbers for GABAergic synaptic density in the *stratum pyramidale* and *stratum radiatum* layers of CA1. Puncta density for A) vGAT and B) gephyrin in the *stratum pyramidale* layer of CA1. Puncta density for C) vGAT and D) gephyrin in the *stratum radiatum* layer of CA1. See Table 2 for individual values. Data obtained from 4-5 slices per animal with 4 animals used per genotype at each age. Symbols are mean ± SEM. WT = wildtype; 2AKO = *Grin2a*$^{-/-}$; Geph = gephyrin.

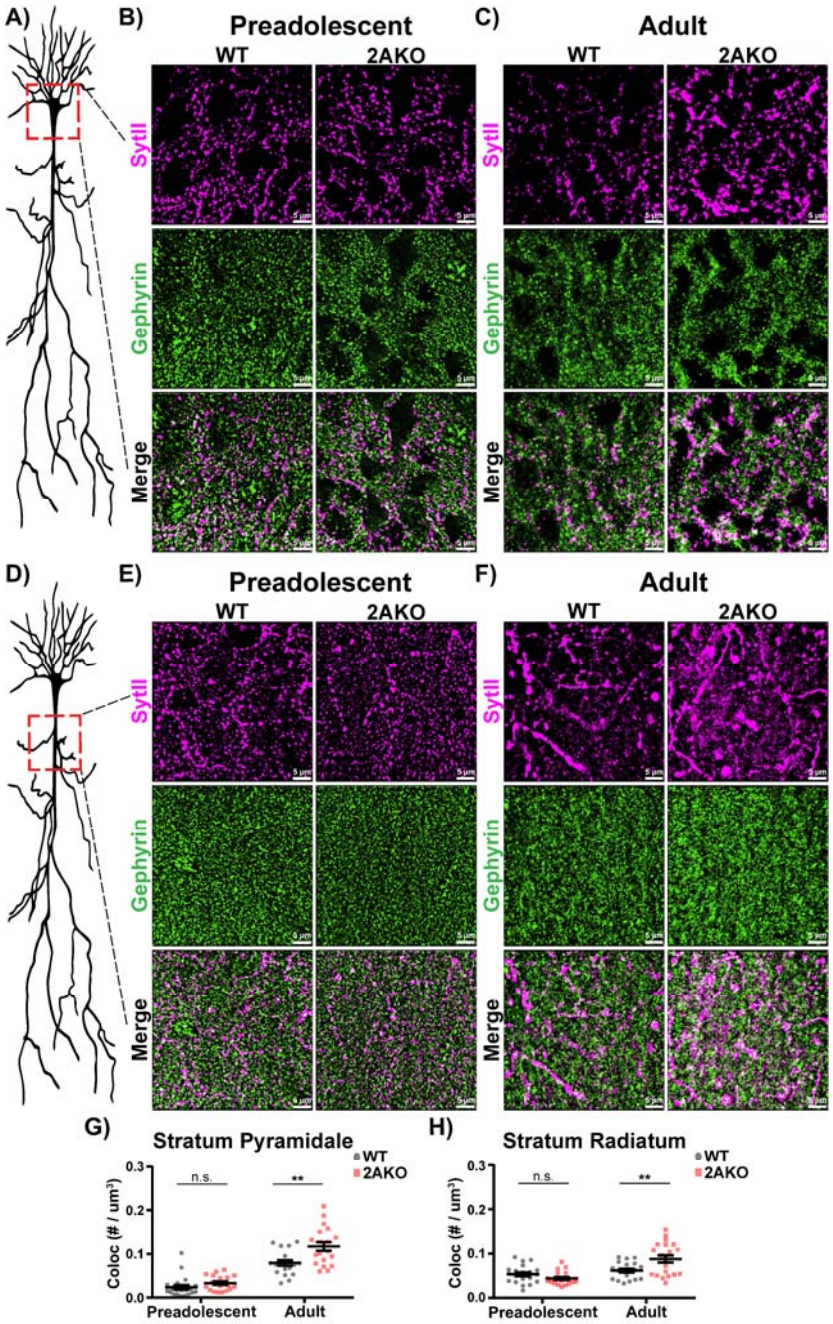

Figure 3. Loss of *Grin2a* causes an age-dependent increase in PV cell-specific synaptic density in the *stratum pyramidale* and *stratum radiatum* layers of CA1. Model pyramidal cell showing that images were captured in the A) *stratum pyramidale* or D) *stratum radiatum* layer of CA1. Representative images of sections stained for SytII (presynaptic) and gephyrin (postsynaptic) GABAergic synaptic markers in the B) preadolescent *stratum pyramidale,* C) adult *stratum pyramidale*, E) preadolescent *stratum radiatum*, and F) adult *stratum radiatum* layers of CA1 in both wild type and *Grin2a*$^{-/-}$ mice. Synaptic density is defined as the colocalization of SytII and gephyrin synaptic markers. G) In the *stratum pyramidale* and H) the *stratum radiatum*, there is an age-dependent increase of PV cell-specific synaptic density in *Grin2a*$^{-/-}$ mice. See Table 2 for individual values. Data obtained from 4-5 slices per animal with 4 animals used per genotype at each age. Symbols are mean ± SEM. WT = wildtype; 2AKO = *Grin2a*$^{-/-}$. SytII = synaptotagmin II; Geph = gephyrin; coloc = SytII/gephyrin colocalized puncta. ** = $p<0.01$; n.s. = not significant.

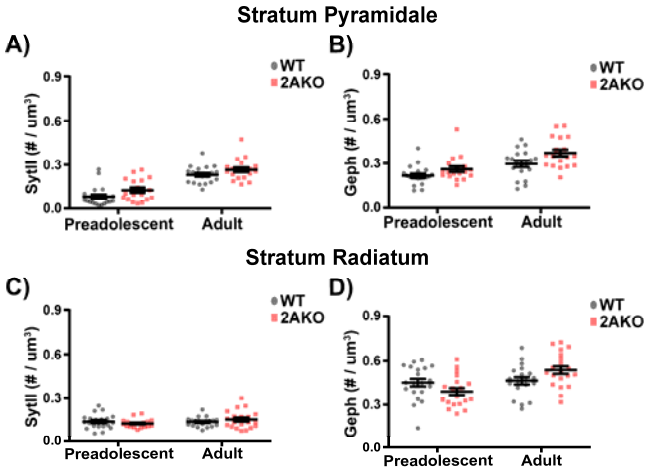

Supplemental Figure 3. Individual puncta numbers for PV cell-specific synaptic density in the *stratum pyramidale* and *stratum radiatum* layers of CA1. Puncta density for A) SytII and B) gephyrin in the *stratum pyramidale* layer of CA1. Puncta density for C) SytII and D) gephyrin in the *stratum radiatum* layer of CA1. See Table 2 for individual values. Data obtained from 4-5 slices per animal with 4 animals used per genotype at each age. Symbols are mean ± SEM. WT = wildtype; 2AKO = *Grin2a*$^{-/-}$. SytII = synaptotagmin II; Geph = gephyrin.

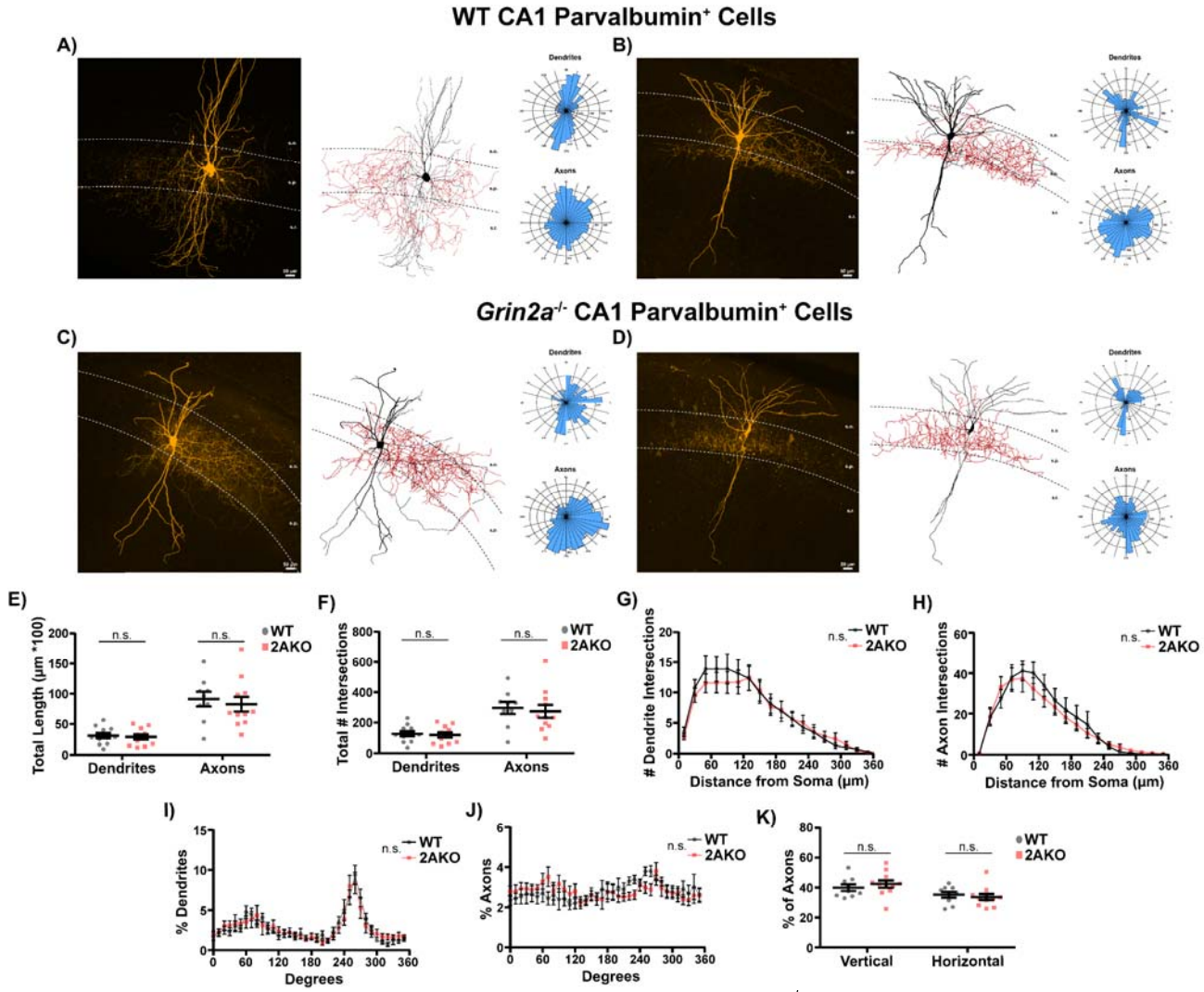

Figure 4. There is no difference in CA1 PV cell morphology in preadolescent *Grin2a*$^{-/-}$ mice. Representative images for A-B) WT or C-D) *Grin2a*$^{-/-}$ biocytin backfilled CA1 PV cells shown as maximum intensity projection images with accompanying Neurolucida tracings (black for dendrites and red for axons) and polar plots for both dendrites and axons. There is no change in E) total length of dendrites or axons or in F) the total number of sholl intersections in dendrites or axons in preadolescent CA1 PV cells from either genotype. Sholl analysis of both G) dendrites and H) axons from preadolescent CA1 PV cells are also unchanged across genotype. The placement of both I) dendrites or J) axons assessed via polar plots showed no differences, with K) equal axonal placement in both the vertical and horizontal planes. Data obtained from 9-11 slices across 4 animals per genotype. Symbols are mean ± SEM. WT = wildtype; 2AKO = *Grin2a*$^{-/-}$. n.s. = not significant. s.o. = *stratum oriens*; s.p. = *stratum pyramidale*; s.r. = *stratum radiatum*

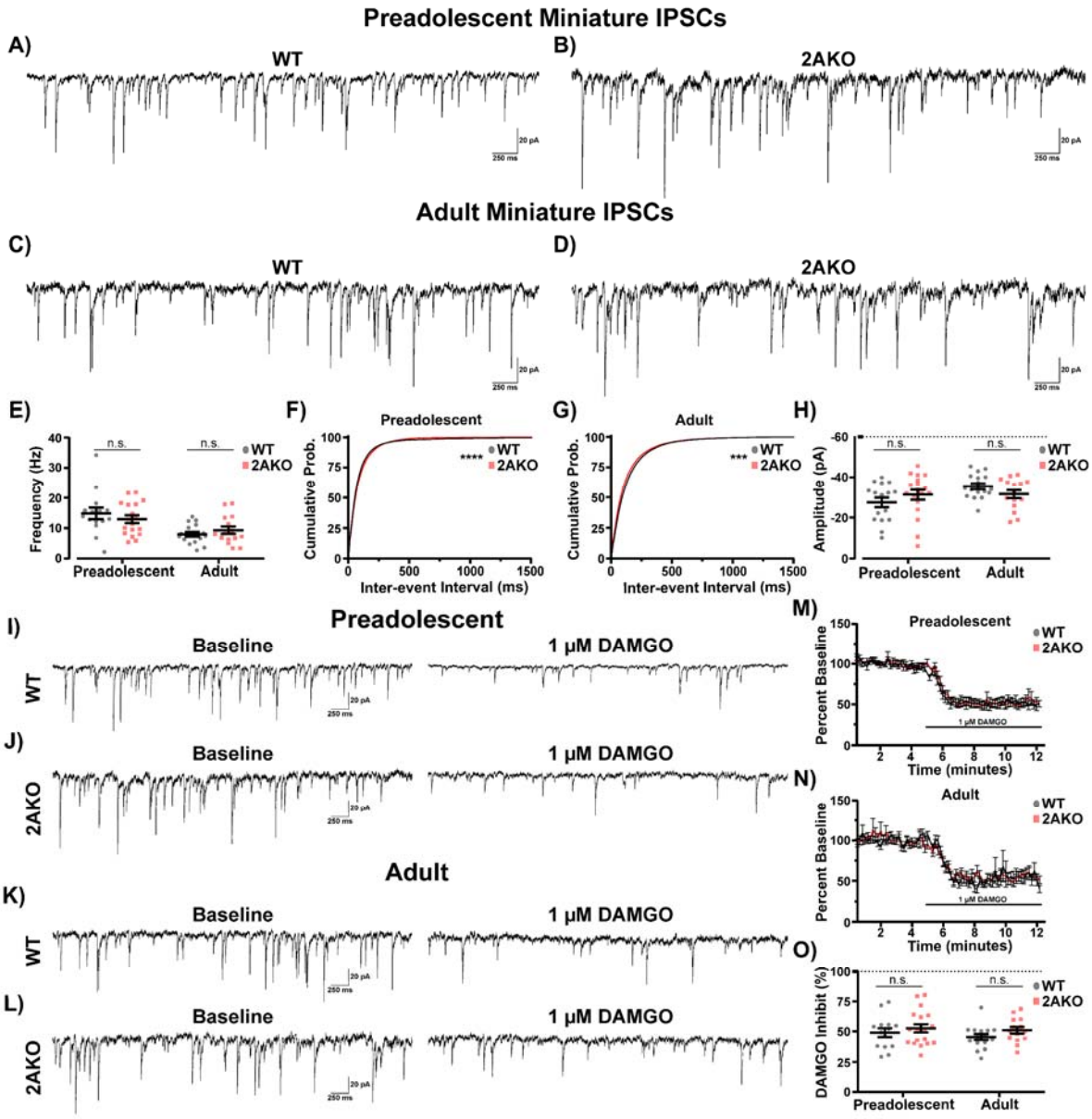

Figure 5. mIPSCs onto CA1 pyramidal cells and DAMGO inhibition of mIPSCs are not changed in *Grin2a*$^{-/-}$ mice. Representative traces of miniature inhibitory postsynaptic currents (mIPSCs) onto CA1 pyramidal cells in preadolescent A) WT and B) *Grin2a*$^{-/-}$ mice, as well as adult C) WT and D) *Grin2a*$^{-/-}$ mice. E) There is no change in mIPSC frequency in *Grin2a*$^{-/-}$ mice at either age. The cumulative probability of mIPSC inter-event interval is significantly altered in *Grin2a*$^{-/-}$ mice at F) preadolescence ($p<0.00001$, Kolmogorov-Smirnov test) and G) adulthood ($p=0.00013$, Kolmogorov-Smirnov test). H) mIPSC amplitude is also unchanged in *Grin2a*$^{-/-}$ mice at both ages tested. Representative traces of mIPSCs before and after bath application of 1 μM DAMGO in preadolescent I) WT and J) *Grin2a*$^{-/-}$ mice, as well as adult K) WT and L) *Grin2a*$^{-/-}$ mice. Timeline showing DAMGO inhibition as a percentage of mIPSC baseline frequency, indicating that responses reached steady-state levels in both M) preadolescent and N) adult mice. O) There is no change in percent DAMGO inhibition of baseline mIPSC frequency in *Grin2a*$^{-/-}$ mice at either age tested. Symbols are mean ± SEM. WT = wildtype; 2AKO = *Grin2a*$^{-/-}$. *** = $p<0.001$; **** = $p<0.0001$; n.s. = not significant.

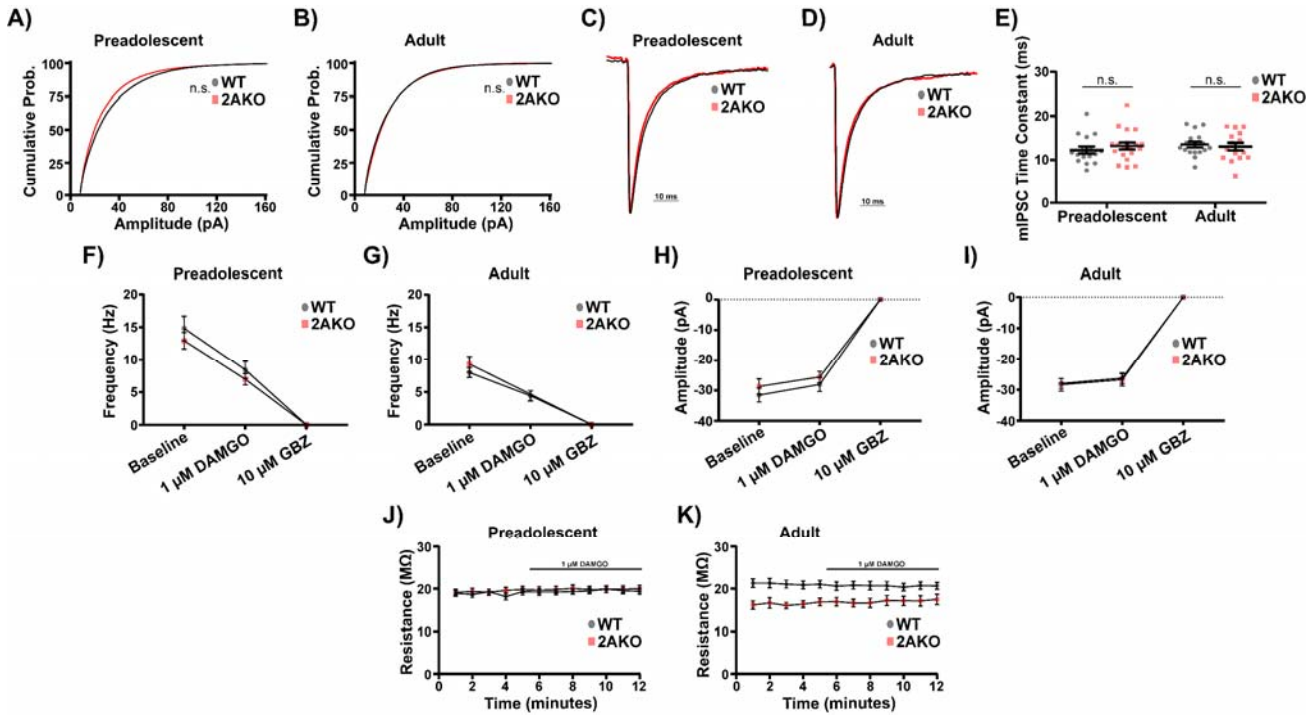

Supplemental Figure 5. Time course and amplitude of mIPSCs onto CA1 pyramidal cells are unchanged in *Grin2a*$^{-/-}$ mice. The cumulative probability distribution plots of mIPSC amplitude in A) preadolescent and B) adult mice are not significantly different between WT and *Grin2a*$^{-/-}$ mice. Representative traces of amplitude-normalized mIPSC traces in C) preadolescent and D) adult mice. E) Weighted mIPSC time constant (see Methods) is unchanged in WT and *Grin2a*$^{-/-}$ mice at either age. Plots showing the average mIPSC frequency in F) preadolescent and G) adult mice indicating raw frequency numbers at baseline, after 1 µM DAMGO application, and after 10 µM gabazine application. Plots showing the average mIPSC amplitude in F) preadolescent and G) adult mice indicating raw amplitude numbers at baseline, after 1 µM DAMGO application, and after 10 µM gabazine application. Temporal plot of series resistance, measured by injecting a 5-mV square pulse every 30 seconds during recording, indicates that data from J) preadolescent and K) adult mice are not impacted by changes in recording conditions or seal quality. Symbols are mean ± SEM. WT = wildtype; 2AKO = *Grin2a*$^{-/-}$; GBZ = gabazine.

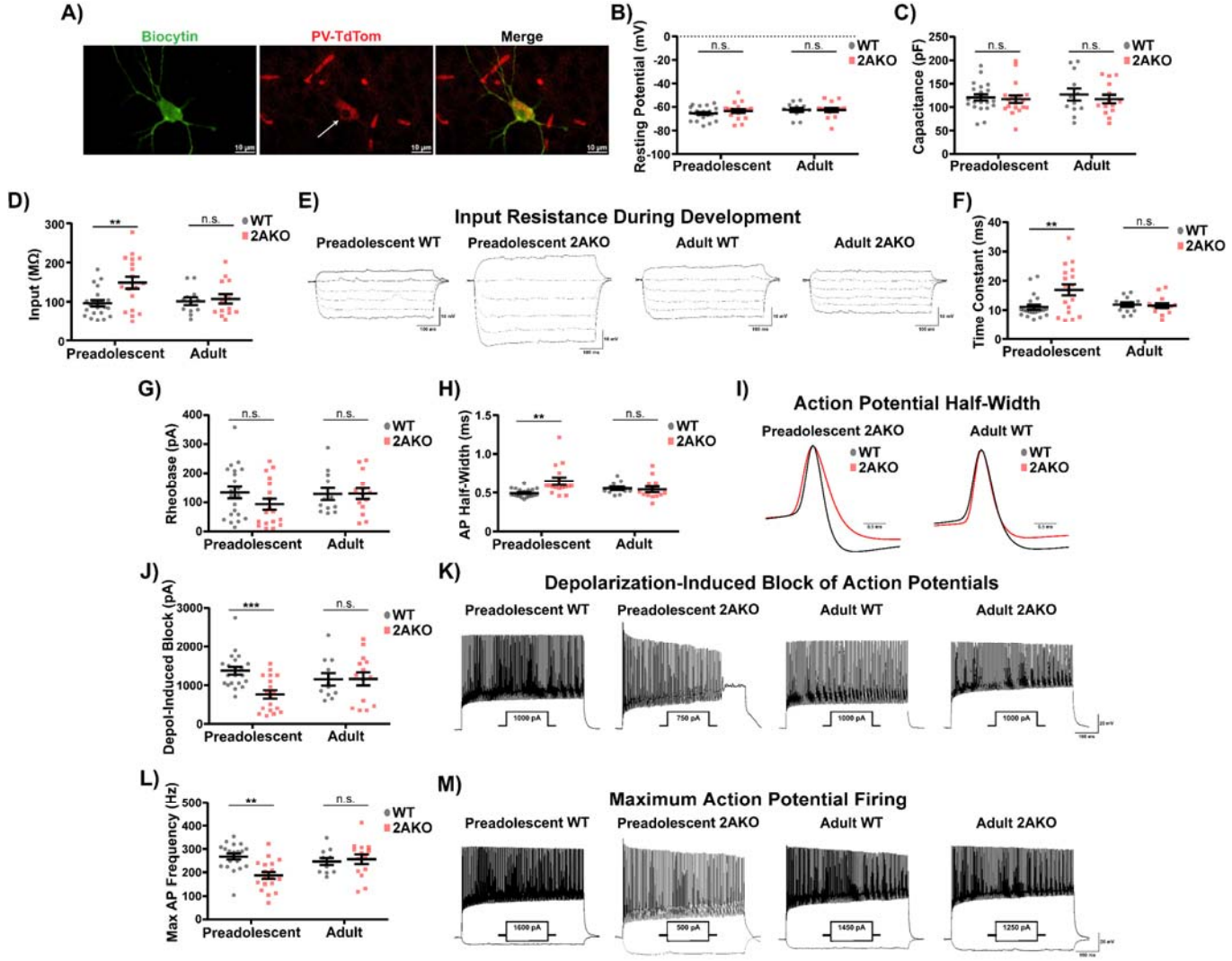

Figure 6. The loss of *Grin2a* in CA1 PV cells causes a transient delay in electrophysiological maturation and dampened action potential signaling. A) Representative images showing that PV-TdTom mice successfully label PV cells in the CA1 subfield. There are no changes in B) resting membrane potential or C) capacitance of PV cells in *Grin2a*$^{-/-}$ mice at either age. D) Input resistance is transiently increased in preadolescent *Grin2a*$^{-/-}$ mice (96.0 ± 7.9 WT vs 149 ± 15 *Grin2a*$^{-/-}$ MΩ; p=0.0032, Student's two-sample t-test), returning to WT levels in adulthood. E) Representative traces from CA1 PV cell voltage deflections in response to a series of current injections used to measure input resistance indicates that preadolescent *Grin2a*$^{-/-}$ mice have an exaggerated voltage response. F) Membrane time constant is transiently increased in preadolescent *Grin2a*$^{-/-}$ mice (11 ± 0.9 WT vs 17 ± 1.9 *Grin2a*$^{-/-}$ ms; p=0.0058, Student's two-sample t-test), returning to WT levels in adulthood. G) There is no change in rheobase in *Grin2a*$^{-/-}$ mice at either age. H) Action-potential half-width is transiently prolonged in preadolescent *Grin2a*$^{-/-}$ mice (0.49 ± 0.01 WT vs 0.65 ± 0.05 *Grin2a*$^{-/-}$ ms; p=0.0018, Student's two-sample t-test), returning to WT levels during adulthood. I) Representative traces of amplitude-normalized action-potential waveforms from WT and *Grin2a*$^{-/-}$ mice in both preadolescents and adults, highlighting the prolonged time course from preadolescent *Grin2a*$^{-/-}$ mice. J) Current required to reach depolarization-induced block is transient diminished in preadolescent *Grin2a*$^{-/-}$ mice (1,374 ± 98 WT vs 761 ± 106 *Grin2a*$^{-/-}$ pA; p=0.0001, Student's two-sample t-test), returning to WT levels in adulthood. K) Representative traces indicating that CA1 PV cells from preadolescent *Grin2a*$^{-/-}$ fail to sustain firing at current injections above 1,000 pA. L) The maximum action potential frequency achieved before depolarization-induced block in diminished in preadolescent *Grin2a*$^{-/-}$ mice (268 ± 13 WT vs 186 ± 15 *Grin2a*$^{-/-}$ Hz; p=0.0002, Student's two-sample t-test), returning to WT levels in adulthood. M) Representative traces of action-potential trains indicates that all but CA1 PV cells from preadolescent *Grin2a*$^{-/-}$ reach a higher frequency of action potential firing before depolarization-induced block. Symbols are mean ± SEM. WT = wildtype; 2AKO = *Grin2a*$^{-/-}$. ** = p<0.01; *** = p<0.001; n.s. = not significant.

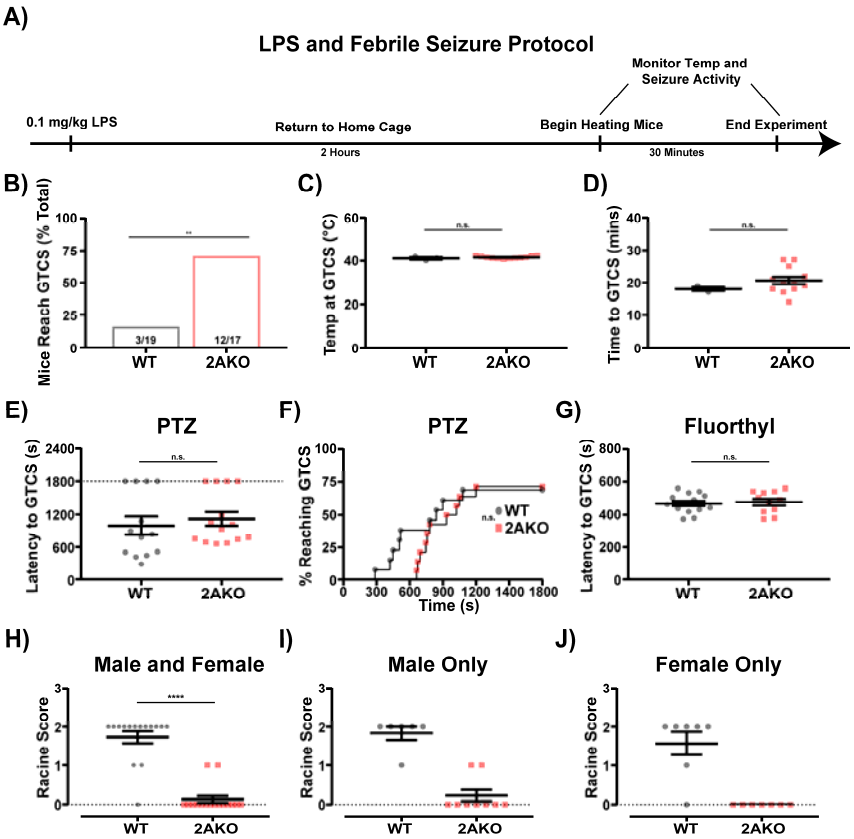

Figure 7. *Grin2a*$^{-/-}$ mice have an aberrant seizure threshold. A) Diagram of protocol designed to elicit seizure activity from a bacterial infection-induced fever. B) Neonatal (P12-15) *Grin2a*$^{-/-}$ mice are more likely to experience generalized tonic-clonic seizures when exposed to 0.1 mg/kg lipopolysaccharide injection and heat (3/19 WT mice vs 13/17 *Grin2a*$^{-/-}$ mice; p=0.0003, chi-squared test). C) Temperature and D) time to generalized tonic-clonic seizure are unchanged between WT and *Grin2a*$^{-/-}$ mice. E) and F) Latency to generalized tonic-clonic seizure is unchanged in adult *Grin2a*$^{-/-}$ mice after 100 mg/kg subcutaneous pentylenetetrazol injection. Dashed line at 1,800 seconds in E) represents mice that did not have a seizure. G) Latency to generalized tonic-clonic seizure is unchanged in adult *Grin2a*$^{-/-}$ mice following inhalation of flurothyl at 20 µL/min. Data in E-G represent data from both genders; individual gender data can be found in supplemental. H) Racine score following 24 mA corneal stimulation at 6 Hz is decreased in adult *Grin2a*$^{-/-}$ mice (median Racine 2 for WT vs 0 for 2AKO; p=0.000001, Mann-Whitney test). I) and J) Decrease in 6 Hz Racine score in *Grin2a*$^{-/-}$ mice appears to be independent of gender. Symbols are mean ± SEM. WT = wildtype; 2AKO = *Grin2a*$^{-/-}$; LPS = lipopolysaccharide; GTCS = generalized tonic-clonic seizure; PTZ = pentylenetetrazol. ** = p<0.01; *** = p<0.001; n.s. = not significant.

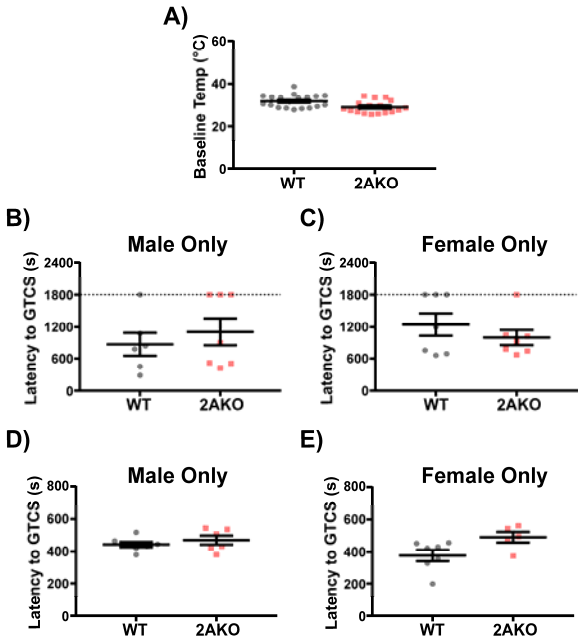

Supplemental Figure 7. Additional seizure assays in *Grin2a*$^{-/-}$ mice. A) There is no detectable difference in baseline temperature 2 hours after 0.1 mg/kg lipopolysaccharide injection measured immediately before heating in WT and *Grin2a*$^{-/-}$ mice. There is no detectable difference in latency to generalized tonic-clonic seizure after 100 mg/kg pentylenetetrazol injection in B) male or C) female mice. Dashed line at 1,800 seconds in B) and C) represents mice that did not have a seizure. There is no detectable difference in latency to generalized tonic-clonic seizure after inhalation of flurothyl at 20 L/min in D) male or E) female mice. Symbols are mean ± SEM. WT = wildtype; 2AKO = *Grin2a*$^{-/-}$; GTCS = generalized tonic-clonic seizure; PTZ = pentylenetetrazol.